PCCP

PERSPECTIVE

View Article Online
View Journal | View Issue

Cite this: *Phys. Chem. Chem. Phys.*, 2015, **17**, 24513

Controlling the physics and chemistry of binary and ternary praseodymium and cerium oxide systems

Gang Niu,[ab] Marvin Hartwig Zoellner,[ab] Thomas Schroeder,*[ab] Andreas Schaefer,[c] Jin-Hao Jhang,[c] Volkmar Zielasek,[c] Marcus Bäumer,*[c] Henrik Wilkens,[d] Joachim Wollschläger,*[d] Reinhard Olbrich,[d] Christian Lammers[d] and Michael Reichling*[d]

Rare earth praseodymium and cerium oxides have attracted intense research interest in the last few decades, due to their intriguing chemical and physical characteristics. An understanding of the correlation between structure and properties, in particular the surface chemistry, is urgently required for their application in microelectronics, catalysis, optics and other fields. Such an understanding is, however, hampered by the complexity of rare earth oxide materials and experimental methods for their characterisation. Here, we report recent progress in studying high-quality, single crystalline, praseodymium and cerium oxide films as well as ternary alloys grown on Si(111) substrates. Using these well-defined systems and based on a systematic multi-technique surface science approach, the corresponding physical and chemical properties, such as the surface structure, the surface morphology, the bulk–surface interaction and the oxygen storage/release capability, are explored in detail. We show that specifically the crystalline structure and the oxygen stoichiometry of the oxide thin films can be well controlled by the film preparation method. This work leads to a comprehensive understanding of the properties of rare earth oxides and highlights the applications of these versatile materials. Furthermore, methanol adsorption studies are performed on binary and ternary rare earth oxide thin films, demonstrating the feasibility of employing such systems for model catalytic studies. Specifically for ceria systems, we find considerable stability against normal environmental conditions so that they can be considered as a "materials bridge" between surface science models and real catalysts.

Received 19th April 2015,
Accepted 20th August 2015

DOI: 10.1039/c5cp02283e

www.rsc.org/pccp

I. Introduction

In Earth's crust, a family of relatively abundant elements are the rare earth elements (REEs, 15 lanthanides La to Lu as well as Sc and Y) accounting for 0.01% of the mass of all elements. REEs are generally reactive with respect to oxygen in the ambient atmosphere so that rare earth oxides (REOs) are mostly stable compounds. In fact, REEs were discovered as oxides being extraordinarily stable, which leads to the "*earth*" part of their name: in early Greek "*earth*" is defined as materials that could not be changed further by heating. The chemical and physical properties of REEs are rather similar and hard to separate from each other, which results in the "rare" part of their name, referring to the difficulty in obtaining the pure element.[1]

REOs exhibit a wide range of fascinating physical and chemical properties and attract intense scientific interest as well as interest with respect to many applications. An important field of application of REOs is heterogeneous catalysis. For example, each year millions of tons of REO raw materials (in which more than 95% is La_2O_3) are utilised as catalysts for cracking of crude petroleum. REOs can also catalyse many other organic reactions and they form important ingredients in automobile exhaust-gas conversion catalysts.[2] In fact, REOs are considered as the most active and selective catalysts for oxidative coupling of methane to form higher hydrocarbon products, a significant process in natural gas processing.[3] Furthermore, REOs are widely used for optical applications.[4] For instance, a mixture of europium and yttrium oxides offers a brilliant-red phosphor.[5] REOs are significant in the glass industry to polish or to dope glass; they are also used as luminescence materials,[6] optical coatings[7] and laser active materials.[4] In the microelectronics domain, there has been burgeoning interest since the 1990s in nanometre scale thin

[a] *IHP, Im Technologiepark 25, 15236 Frankfurt(Oder), Germany. E-mail: schroeder@ihp-microelectronics.com*
[b] *BTU Cottbus-Senftenberg, Institute of Physics, Konrad-Zuse-Str. 1, 03046 Cottbus, Germany*
[c] *Institute of Applied and Physical Chemistry, University of Bremen, Leobener Str. UFT, 28359 Bremen, Germany. E-mail: mbaeumer@uni-bremen.de*
[d] *Fachbereich Physik, Universität Osnabrück, Barbarastr. 7, 49076 Osnabrück, Germany. E-mail: reichling@uos.de, jwollsch@uos.de*

films of REOs, initially fuelled by the exploration of alternative high dielectric constant (high-κ) gate insulator materials to maintain "Moore's law" predicting an exponential growth of the number of transistors on a chip *via* a continuous scaling of complementary metal–oxide–semiconductor (CMOS) devices.[8] Thanks to their remarkable properties such as high-κ, a large band gap, a large band offset and high thermal stability in combination with Si, REOs were considered as promising high-κ dielectric candidates.[8] Moreover, the capability of growing high quality, epitaxial, single crystalline REO films on Si with a thickness of up to several hundred nanometres opens a pathway for their applications in "More than Moore" technology, namely the integration of more functions on "frozen" Si CMOS chips without further scaling.[9] In this context, REOs not only demonstrate diverse functions beyond conventional semiconductor functionality such as the use as diluted magnetic semiconductors.[10] They can also be used as buffers for the integration of other functional layers such as superconductive,[11] ferromagnetic[12] and multiferroic[13] oxides as well as semiconductors like Si,[14] Ge[15] and III–V[16] grown on Si.

Considering that the structural and chemical properties of REOs can strongly influence their electrical and catalytic characteristics, it is necessary to understand the structure–property relationship to improve their performance in device applications. However, the complex features of REOs like their polymorphism and varying oxygen stoichiometry make the exploration of the structure–property relationship rather difficult. In this context, a surface science approach for studying single crystalline REO films turns out to be a valuable method, because (i) many REO-related scientific issues or applications are focused on the surface properties. (ii) By starting from the well-ordered, flat, two dimensional and stoichiometric single crystalline REO film, one can increase the complexity step by step to understand the structure–property relationship from simple to complex materials. (iii) One can control the surface properties by tailoring thin film properties like thickness and surface morphology as REOs generally possess a high oxygen mobility,[4] leading to a strong coupling between the volume and surface properties of the thin film.

In this paper, we review recent progress in a detailed understanding of the chemistry and physics of two representative REOs, namely ceria and praseodymia. Cerium and praseodymium both form the tetravalent RE dioxides having a fluorite structure (space group $Fm\bar{3}m$, N.225). Based on this basic structure, they form a multitude of other phases due to the reduction of the oxygen content by the formation of oxygen vacancies in the lattice. Oxygen vacancies can be considered as ions with double positive charge and are commonly represented as $V_O^{\bullet\bullet}$ according to the Kröger–Vink notation.[17] $V_O^{\bullet\bullet}$ formation is one of the most important factors determining the properties of oxides because it has a strong impact on the solid state physical properties and, accordingly, the performance in different applications of oxides. The increasing formation of $V_O^{\bullet\bullet}$ in CeO_2 or PrO_2 is associated with Ce^{4+} to Ce^{3+} and Pr^{4+} to Pr^{3+} reductions, respectively. Interestingly, Ce prefers the +4 valence while Pr favours the +3 valence in the oxides under commonly used preparation conditions, which is a result of the electrochemical reduction potential of Ce^{4+}/Ce^{3+} (1.74 eV) being considerably smaller than that of Pr^{4+}/Pr^{3+} (3.2 eV).[18] Combining Ce and Pr oxides enables us to tailor the properties of oxides such as the oxygen mobility and the oxygen storage capacity. Therefore, we include two types of combined oxide systems in our study, namely CeO_2/Pr_2O_3 bilayers and $Ce_{1-x}Pr_xO_{2-\delta}$ mixed oxide films.

Fig. 1 shows the bulk phase diagrams of the Ce–O and Pr–O systems.[19] Analysing the phase diagrams reveals general features that (i) almost all structures can be considered as quasi-cubic ones despite the existence of different non-stoichiometric phases, (ii) all structures are related to either a random or a periodic arrangement of $V_O^{\bullet\bullet}$, (iii) the lattice constant increases as the oxygen content decreases because the cation radii increase with a lower oxidation state[20,21] and (iv) the composition of the oxides strongly depends on thermodynamic and kinetic factors, *i.e.* the temperature as well as the physical state and preparation history.

Rare earth oxides have been studied for a long time and the present work can build on a solid stock of fundamental

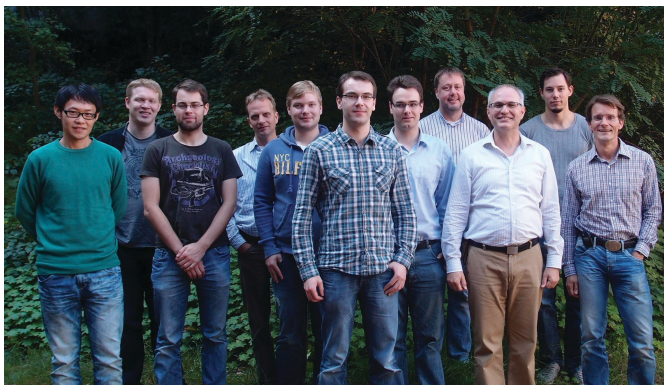

The research team behind the cooperative work presented in this paper. From left to right: Jin-Hao Jhang, Sebastian Gevers, Henrik Wilkens, Volkmar Zielasek, Christian Lammers, Hans-Hermann Pieper, Reinhard Olbrich, Joachim Wollschläger, Michael Reichling, Marvin Hartwig Zoellner and Marcus Baumer. Missing from the photo: Gang Niu, Andreas Schaefer and Thomas Schroeder

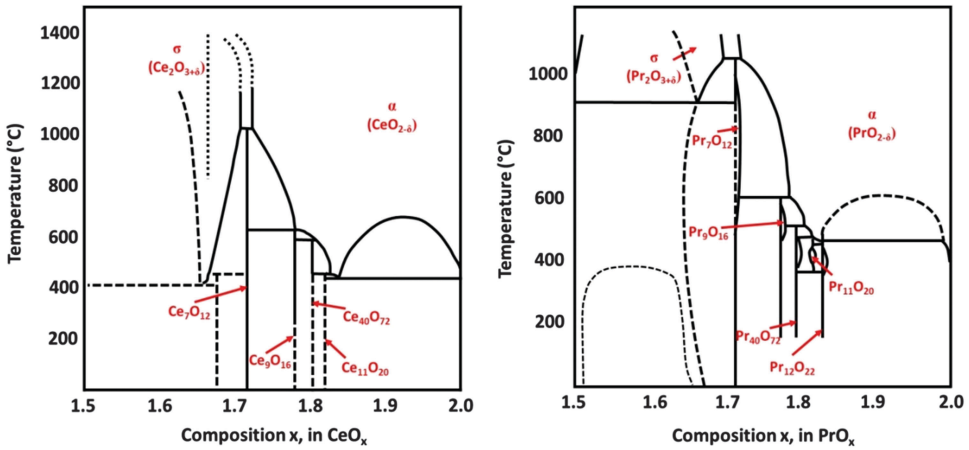

Fig. 1 Bulk phase diagrams for the systems Ce–O (left) and Pr–O (right). (Reproduced from ref. 19.)

knowledge on the physics and chemistry of these materials. Due to their outstanding role in chemical catalysis,[22] the vast majority of publications in the field have been devoted to ceria where many fundamental questions related to surfaces and near-surface processes have been addressed. Related experimental and theory studies of recent years comprise the preparation of surfaces, their morphology and atomic structure,[23–27] surface characterisation,[28–34] surface defects with an emphasis on vacancies and their arrangement[35–46] as well as investigations on adsorbates[47–59] and metal atoms or clusters[41,60–70] on ceria surfaces.

In model catalysis, the approach to grow a thin oxide film on a metal support has been widely employed to study the catalytic properties of REO systems.[71] To model the REO systems by such thin film studies for gaining an in-depth understanding of the structure–reactivity correlation, high quality crystalline oxides are required. Several preparation methods have been studied, such as pulsed laser deposition (PLD),[11] chemical vapour deposition (CVD),[72] atomic layer deposition (ALD)[73] and molecular beam epitaxy (MBE).[74]

The method of choice to grow REO films for the studies presented here is MBE on silicon substrates in combination with annealing in various environments including a vacuum, N_2 or O_2 atmosphere as well as oxygen-plasma-treatment. This preparation method has many advantages over other approaches, namely

- The method allows film growth on large samples (4 inch Si wafers) thus producing many samples with very similar properties from one batch suitable for surface science characterisation tools with sample stages typically 1 cm^2 in size.
- The nature of the MBE technique provides good interface and stoichiometry control (including ternary alloys) as well as the possibility of *in situ* film growth monitoring by reflected high energy electron diffraction (RHEED) and X-ray photoemission spectroscopy (XPS), thus ensuring the realisation of high quality single crystalline films.
- Annealing in different atmospheres and in the ultra-high vacuum provides access to clean surfaces and various oxygen stoichiometries.

The produced film systems provide a multitude of research possibilities such as

- oxidation state and structural flexibility by exploiting the full range of PrO_x and CeO_x with x = 1.5–2,
- thickness dependence studies that help to clarify the role of oxygen exchange between the surface and bulk,
- stoichiometry studies with ternary systems,
- tailoring the morphology and nanostructure over a wide range of surface structures, and
- model system studies to explore new physical phenomena in materials like room temperature ferromagnetism.

It is important to note that this approach fundamentally differs from the growth of ultra-thin films on metal surfaces often used for surface science studies in this field.[75–88] While basic atomic and defect structures of ultra-thin films can be assumed to be similar to surfaces of bulk oxide crystals, the ultra-thin film does not provide a significant reservoir of oxygen that is important for understanding surface processes depending on an interaction between the surface and volume. For this reason, in the context of the work reported here, mostly films of a thickness ranging from some tens to some hundreds of nm are used rather than films having a thickness of only a few atomic layers.

Single crystalline binary and ternary epitaxial ceria and praseodymia films are characterized by a multitude of techniques including high-resolution transmission electron microscopy (HRTEM), X-ray diffraction (XRD), synchrotron based grazing incidence X-ray diffraction (SR-GIXRD), X-ray specular reflectivity (XRR), synchrotron based X-ray absorption fine structure (SR-XAFS), X-ray photoelectron spectroscopy (XPS), Auger electron spectroscopy (AES), synchrotron radiation based photoelectron spectroscopy (SR-PES), spot profile analysis of low energy electron diffraction patterns (SPA-LEED), non-contact atomic force microscopy (NC-AFM), Kelvin probe force microscopy (KPFM) and temperature-programmed desorption (TPD) to explore the film bulk structure, interface and surface structures, surface morphology, local polarisation, adsorption properties and surface reactivity.

The paper is organized in sections, each covering a certain system or aspect of REO film growth or characterisation.

In Section II we introduce the experimental details of film growth and post-deposition annealing processes. In Section III we present the results and discussion regarding the thin film structure (III.1) as well as the surface structure and morphology (III.2). Each of these sections is structured into sub-sections covering pure praseodymia and ceria phases, trivalent systems and phase transitions due to film reduction. Surface adsorption of methanol on pure and mixed systems in different reduction states is investigated with the results presented in Section IV. The main conclusions to be drawn from the entire work are summarized in Section V.

II. Experiment

Here, we focus on the film fabrication method and post-deposition annealing (PDA) processes. Information on the characterisation experiments can be found in the respective sections and references therein.

II.1 Film growth

Before being introduced into the MBE growth chamber, boron-doped (10^{15} cm^{-3}) p-type, 4-inch Si(111) substrates (ρ typically 10 Ω cm) are chemically cleaned using the following procedures to obtain an atomically smooth Si surface. The application of the standard Piranha process[89] is followed by 30 min etching in 40% NH_4F and finally 10 min rinsing in de-ionised water.[90] Subsequently, the H-terminated Si(111) wafers are annealed in UHV for 5 min at 750 °C to prepare a clean (7 × 7) reconstructed Si(111) surface. The oxide thin film growth is carried out using an electron beam evaporation method. Highly purified oxide materials (Pr_6O_{11} or CeO_2) filled in carbon crucibles are bombarded by a high energy electron beam. Note that Pr_6O_{11} is reduced to Pr_2O_3 in the crucible before evaporating. The growth of the oxides occurs at a rate of 0.05 to 0.1 nm s^{-1}. Different from Si and Ge targets which melt under electron bombardment thus providing a stable evaporation rate, oxide materials in the crucible often do not melt resulting in an instable evaporation rate. The stability of the oxide growth rate is, therefore, controlled using a quartz crystal microbalance (QCM) sensor regulating the e-beam filament current for each electron gun controller. This also allows the measurement of the real time growth rate. The typical substrate temperature and oxygen partial pressure during the growth are 625 °C and 10^{-7} to 10^{-5} mbar, respectively. The film thickness is homogeneous over the whole 4-inch wafer and can be well controlled resulting in reproducible preparation results. For studies presented here, the film thickness is varied from 10 to 200 nm. For the preparation of ceria samples, a 1 nm thick Pr_2O_3 film is deposited on the Si substrate as a buffer layer before the growth of ceria to avoid amorphous SiO_2 formation in the initial stages of epitaxial growth and to ensure single crystallinity of the ceria films.[74] The mixed oxide films are prepared by co-evaporating the oxide materials in crucibles where the Ce/Pr ratio is tuned by adjusting the growth rate of each oxide.

II.2 Post-deposition annealing

Different post-deposition annealing (PDA) processes are employed on the oxide/Si samples for different objectives, as illustrated by Fig. 2. Generally, post-deposition reduction processes are carried out on CeO_2/Si(111) samples to obtain different CeO_x phases while post-deposition oxidation processes are performed on Pr_2O_3/Si(111) samples to realise different PrO_x phases. PDA treatments can be categorized as follows:

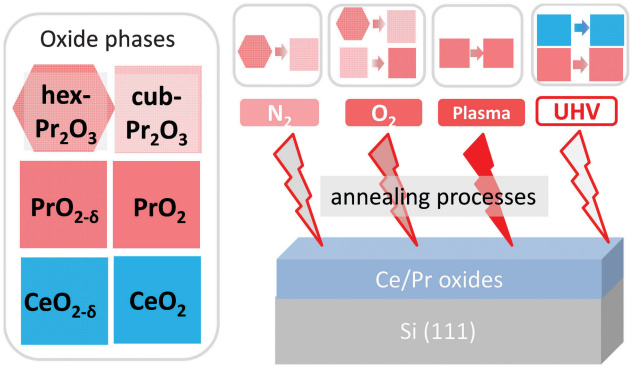

Fig. 2 Illustration of effects of different PDA processes on the oxide phases.

(1) N_2-annealing. Annealing in a tubular furnace at 870 K under 1 bar N_2 for 5 min. This method is used to induce a phase transition from the Pr_2O_3 hexagonal phase (hex-Pr_2O_3) to the cubic phase (cub-Pr_2O_3).[91]

(2) O_2-annealing. Annealing in a tubular furnace at 670 K under 1 bar O_2 for 30 min. This treatment can lead not only to a Pr_2O_3 hexagonal to cubic phase transition but also to a Pr_2O_3 to $PrO_{2-\delta}$ phase transition.[92]

(3) Oxygen-plasma-treatment. A specially designed UHV-compatible, capacitively coupled radio frequency (RF) plasma source[93] is used to fully oxidise defective PrO_2 films.[94,95] Here, the sample is inserted into the phase electrode of the capacitor and, thus, its surface is directly exposed to the oxygen-plasma (30 W power) for 30 to 60 min and under a continuous gas flow (15 sccm oxygen). The CeO_2 films were also exposed to an oxygen plasma to clean their surfaces and to improve their crystalline structure. In this case, the plasma is generated by a microwave source (2.45 GHz, 360 W power, 80 sccm gas flow, 0.26 mbar gas pressure) and the sample is exposed for 15 min.

(4) UHV-annealing. Annealing under UHV conditions up to temperatures above 1270 K. This procedure is used to reduce CeO_2 or PrO_2 films.[96,97]

III. Thin film characterization

III.1 Thin film structure

III.1.1 Pure praseodymia phases

A. hex-Pr_2O_3. The sesquioxide Pr_2O_3 can crystallise either in a hexagonal or a cubic phase. However, hex-Pr_2O_3(0001) growth is favoured in UHV on Si(111) due to the smaller lateral lattice mismatch of +0.5% compared to +2.7% mismatch for cub-Pr_2O_3(111).[91] Specular XRD θ–2θ measurements on both hex-Pr_2O_3/Si(111) and cub-Pr_2O_3/Si(111) systems (obtained after the hex-to-cub transition due to PDA, see below) are shown in Fig. 3.[74] Both, hex-Pr_2O_3 and cub-Pr_2O_3 films show diffraction

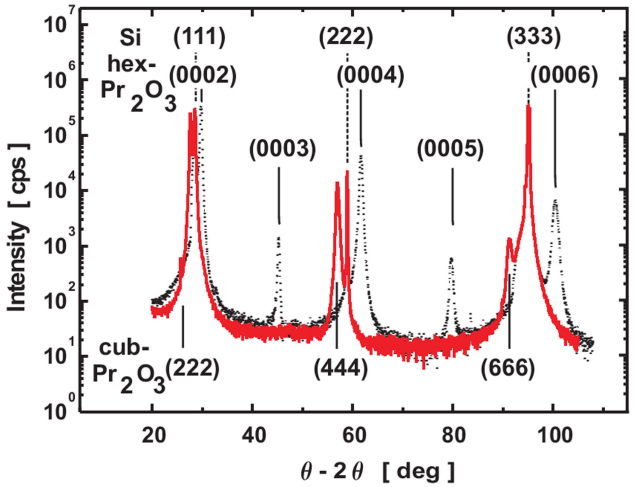

Fig. 3 Specular XRD θ–2θ results for a 50 nm thick as-deposited hex-Pr_2O_3/Si(111) film (dotted line) and the cub-Pr_2O_3/Si(111) structure of the same film after annealing in oxygen (red solid line). Dashed lines indicate Si substrate bulk reflexions. (Reproduced from ref. 102.)

peaks close to Si(hkl) ($h = k = l = 1, 2, 3$) reflections and hex-Pr_2O_3 exhibits additional peaks, *e.g.* hex-Pr_2O_3(0003) and hex-Pr_2O_3(0005). More detailed X-ray diffraction studies[98,99] determine the epitaxial relationship of the hex-Pr_2O_3/Si system as hex-Pr_2O_3(0001); $\langle -1100\rangle \| \mathrm{Si}(111)$; $\langle -1-12\rangle$. As the interface structure and atomic bonding are of particular interest, Jeutter *et al.*[100] analysed this system and concluded that the first layer on Si atoms is an oxygen layer, while the subsequent praseodymium layer prefers to be located above the silicon T4 site rather than the H3 site yielding the ACACAC... stacking sequence of the praseodymium atoms along the (0001) direction illustrated in Fig. 4(a). Initially, the hex-Pr_2O_3 film remains pseudomorphic and grows layer by layer. A relaxation process occurs when the thickness exceeds ~12 nm and is accompanied by a roughening of the surface and a decrease of the domain size. Therefore, the growth follows the Stranski–Krastanov growth mode.[89,101] Furthermore, an atomically sharp interface between Pr_2O_3 and Si is found, as shown in Fig. 4(b) by a cross-sectional HRTEM image of the hex-Pr_2O_3(0001)/Si(111) interface.[102]

B. cub-Pr_2O_3. Because hex-Pr_2O_3(0001)/Si(111) thin films are metastable, it is possible to transform them by N_2 or low pressure O_2 annealing into twin-free, single crystalline type-B oriented cub-Pr_2O_3.[74,91] The epitaxial relationship of the cub-Pr_2O_3/Si(111) system is studied in detail by XRD measurements and found to be cub-Pr_2O_3(111); $\langle 11-2\rangle \| \mathrm{Si}(111)$; $\langle -1-12\rangle$.[91,102] The phase transformation is accompanied by a change in the stacking sequence from ACACAC... to ABCABC... resulting in a type-B orientation. Fig. 5(a) shows the type-B cub-Pr_2O_3(111)/Si(111) structure model (upper panel) where praseodymium (red) oxide is connected to the Si(111) substrate through oxygen atoms (yellow). Note, that the first praseodymium layer is also above the silicon T4 site (*cf.* Fig. 4(a)). The bottom panel of Fig. 5(a) shows the registry of Pr and Si atoms in type A (left) and type B (right) interfaces. In a type A interface, Pr atoms from the first oxide layer are located above Si atoms from the second (111) double-layer of Si. In a type B interface, Pr atoms from the first oxide layer are located above Si atoms from the first (111) double-layer of Si. The results from *ab initio* calculations point to a stabilisation of the type-A/B stacking transition at the cub-Pr_2O_3(111)/Si(111) interface by electrostatic interactions.[103] Moreover, an amorphous SiO_x interfacial layer is observed at the cub-Pr_2O_3/Si interface by HRTEM as shown in Fig. 5(b). This interfacial layer is formed during the phase transformation annealing process due to the diffusion of oxygen through the Pr_2O_3 film to the Si surface, especially at elevated temperatures.[102]

C. cub-$PrO_{2-\delta}$. It is well known that for bulk praseodymia, the β-phase Pr_6O_{11} is stable under normal conditions[104] while one has to increase both the oxygen pressure and the oxidation temperature to at least 1 bar O_2 and above 300 °C, respectively, to form the PrO_2 α-phase.[105] Therefore, structural phase transformations due to the exposure of very thin hex-Pr_2O_3 films to 1 bar O_2 for 30 min at a temperature of 400 °C have been studied by means of SR-GIXRD.[92,106] In the following, XRD and GIXRD measurements are presented. h, k, and l values of the indexed peaks are chosen with respect to the bulk lattices of the corresponding material and will be referred to as $(hkl)_B$, whereas labelling of the axes and rods corresponds to the hexagonal Si(111) lattice in surface coordinates $(hkl)_S$. Fig. 6(a) shows specular out-of-plane XRD data (Θ–2Θ scans) obtained from hex-Pr_2O_3 films annealed at different temperatures. Obviously, the spectra obtained for films after annealing below 300 °C differ from those obtained after annealing at higher temperatures.

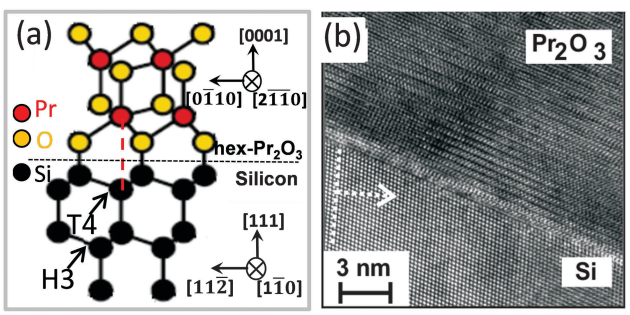

Fig. 4 (a) Atomic model of the hex-Pr_2O_3(0001)/Si(111) interface. (b) Cross-sectional HRTEM image of the hex-Pr_2O_3(0001)/Si(111) interface.

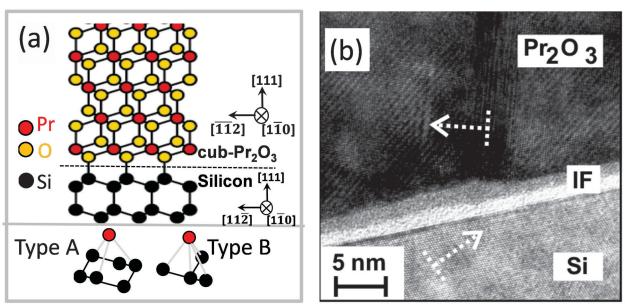

Fig. 5 (a) Atomic model of the cub-Pr_2O_3(111)/Si(111) interface. (b) Cross-sectional HRTEM image of the cub-Pr_2O_3(0001)/Si(111) heterostructure.

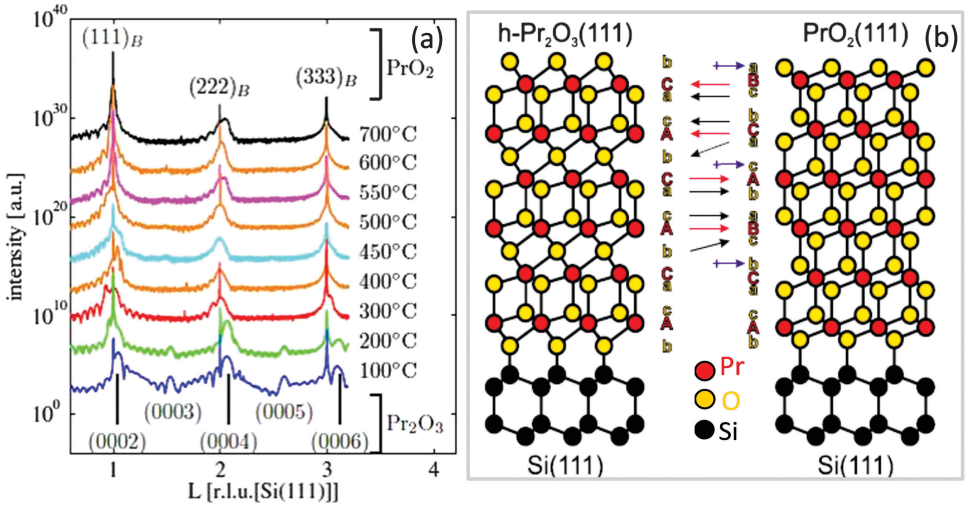

Fig. 6 (a) Specular XRD θ–2θ measurements on a 5 nm thick hex-Pr_2O_3 film after annealing at different temperatures in a 1 bar O_2 atmosphere. (b) Model proposed for the transition from the hex-Pr_2O_3 phase to the cub-Pr_2O_3 phase. (Reproduced from ref. 92.)

The same result is obtained for GIXRD recording CTRs (crystal truncation rods) of higher diffraction order originating from the finite penetration depth of X-rays. We note here that CTRs are the scattering peaks arising between bulk Bragg reflections due to a sharp termination of the crystal lattice at the surface while the direction of CTRs is perpendicular to the surface and is sensitive to the surface/interface structure. An analysis of the Bragg peak positions shows that the films annealed at low temperatures keep the hexagonal structure while films annealed at higher temperatures are transformed into a cubic structure which is B oriented with respect to the Si(111) substrate. Therefore, as shown in Fig. 6(b), the ACACAC... stacking of the Pr sublattice of hex-Pr_2O_3 is transformed to the ABCABC... stacking of the Pr sublattice of PrO_2 having the fluorite structure. In addition, the oxygen sublattice has to be rearranged. Especially, the alternating stacking of oxygen monolayers and bilayers between Pr layers for hex-Pr_2O_3 (denoted in Fig. 6(b) by b and c/a, respectively) is substituted by a homogeneous distribution of oxygen bilayers for PrO_2. Similar to the cation stacking, the oxygen stacking follows the pattern bcabca (*cf.* Fig. 6(b)).

A closer inspection of the specular Bragg peaks presented in Fig. 7(a) shows that a cubic praseodymia film does not exhibit one single phase but consists of two laterally separated phases with different (111) layer distances as sketched in Fig. 7(b). The layer distance of these phases decreases with increasing annealing temperature as expected for increasing oxygen load accompanied by a decreasing cation radius. In-plane scans (not presented) reveal that the lateral lattice constant of the higher oxidised film is pinned to the lateral lattice constant of hex-Pr_2O_3(0001). This effect has been attributed to the excellent lateral lattice matching between hex-Pr_2O_3(0001) and Si(111). Assuming that the praseodymia films are elastically deformed, one can calculate

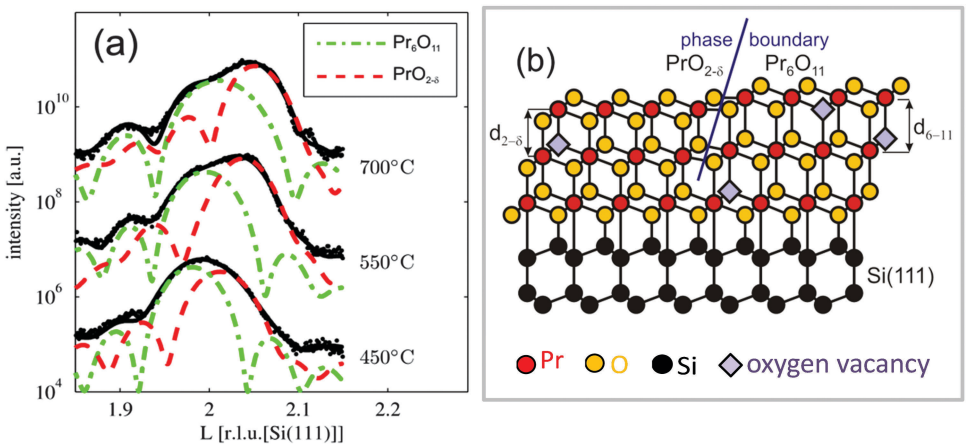

Fig. 7 (a) Close-up of three CTRs presented in Fig. 6(a): praseodymia Bragg peaks are split into two contributions. The Bragg positions are obtained from fitting: with two fitted sub-functions due to the coexistence of Pr_6O_{11} (green line) and $PrO_{2-\delta}$ (red line). (b) Model for the coexistence of Pr_6O_{11} and $PrO_{2-\delta}$ with a lateral phase separation (two column model). The layer distance in Pr_6O_{11}(111) is expanded compared to the one of $PrO_{2-\delta}$(111) due to the larger cation size for the lower (average) oxidation state. (Reproduced from ref. 92 and 106.)

the cubic lattice constant of the undistorted praseodymia depending on the film stoichiometry.[107] Taking into account the Poisson ratio of $\nu = 0.32$ reported by Zaumseil *et al.*,[108] one obtains that the inhomogeneously distributed phases of the cubic praseodymia film have Pr_6O_{11} and $PrO_{2-\delta}$ stoichiometry if the films are annealed at temperatures below 550 °C. After further annealing, the $PrO_{2-\delta}$ phase is transformed into PrO_2 while the coexisting Pr_6O_{11} phase is transformed into $PrO_{2-\delta}$ when annealing at temperatures above 600 °C. Therefore, after this treatment, the praseodymia film exhibits both laterally coexisting $PrO_{2-\delta}$ and PrO_2 phases. With respect to the Si(111) substrate, $PrO_{2-\delta}$ as well as PrO_2 are aligned by $PrO_x(111)$; $\langle 11-2\rangle$ ||Si(111); $\langle -1-12\rangle$.

The results from XRR studies show that the previously sharp interface between the hex-Pr_2O_3(0001) film and the Si(111) substrate is dissolved and a praseodymium silicate with increasing thickness evolves after annealing at temperatures above 500 °C.[91] The silicate interface layer consumes more and more of the praseodymia film with increasing annealing temperature. Therefore, oxidation by molecular oxygen has to be performed at temperatures below 500 °C to minimize the formation of interface silicate and alternative methods have to be applied to completely oxidise the praseodymia film.

D. PrO_2. The oxidation process can be accelerated by exposing the film to an oxygen plasma. Therefore, cubic praseodymia films oxidized in molecular oxygen at annealing temperatures below 500 °C are exposed to a cold RF plasma[94] to study this effect. Synchrotron based XRD studies shown in Fig. 8 demonstrate that the oxygen plasma treated praseodymia films exhibit two laterally coexisting phases of $PrO_{2-\delta}$ and PrO_2 stoichiometry. Taking into account the elastic deformation of the film due to lateral pinning at the interface (lateral lattice constant of hex-Pr_2O_3, *cf.* above) the extrapolated cubic lattice constants are 540.4 pm and 538.6 pm for $PrO_{2-\delta}$ and PrO_2, respectively. For comparison, a lattice constant of 539.2 pm has been reported for bulk PrO_2 after annealing at 720 °C in 92 bar O_2.[109] Thus, a higher oxygen load is obtained by plasma oxidation compared to oxidation in molecular oxygen at high pressure. Furthermore, a detailed analysis of the XRD data within the kinematic diffraction theory shows that a very thin crystalline Pr_6O_{11} layer (thickness less than 2 nm) is stabilized at the interface even when the residual film is completely oxidised.

III.1.2 Bilayer heterostructures. A high oxygen storage capacity as well as a good ion mobility are outstanding properties of CeO_2 and PrO_x.[110–112] By combining the two oxides in a layered system, one can observe oxygen exchange between the two materials. We, therefore, perform a study on bilayer heterostructures combining CeO_2 and Pr_2O_3. High quality, type-B oriented CeO_2 films are grown on both, cub- and hex-Pr_2O_3 buffer layers on a Si(111) substrate.[26] Fig. 9(a) and (b) show XRD results of laboratory-based specular θ–2θ measurements on both stacks and SR-GIXRD measurements on CeO_2/hex-Pr_2O_3/Si(111), respectively. The in-plane and out-of-plane epitaxial relationships are given by $CeO_2(111)$; $\langle 11-2\rangle$‖cub-$Pr_2O_3(111)$; $\langle 11-2\rangle$‖Si(111); $\langle -1-12\rangle$ and $CeO_2(111)$; $\langle 11-2\rangle$‖hex-$Pr_2O_3(0001)$; $\langle -1100\rangle$‖Si(111);

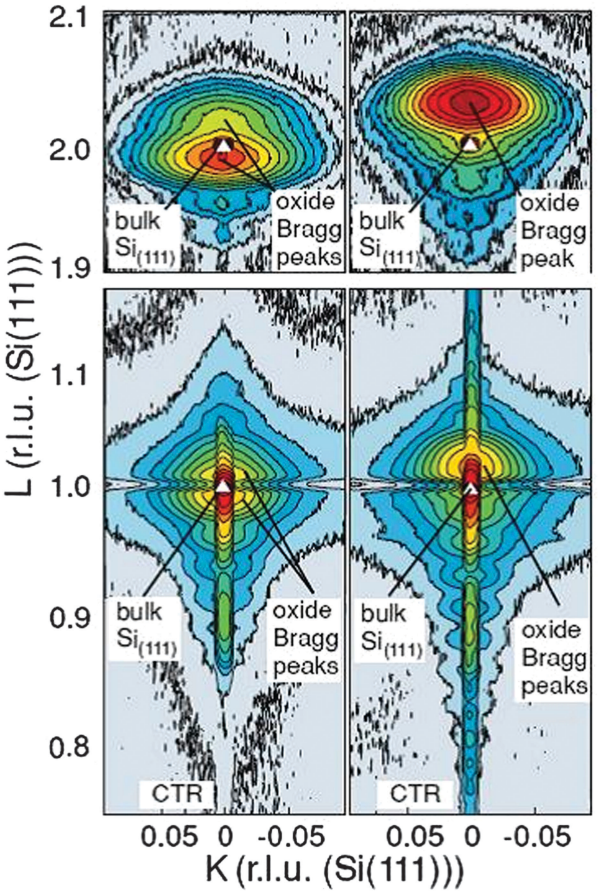

Fig. 8 Reciprocal space maps close to the (111) Bragg peak (bottom) and (222) Bragg peak (top) of 15 nm thick praseodymia films investigated by SR-GIXRD. Left side: praseodymia film after oxidation in 1 atm oxygen. Right side: praseodymia film after oxygen plasma treatment. Clearly, the position of the praseodymia Bragg peaks shift due to the reduced lattice constant after the incorporation of oxygen. (Reproduced from ref. 95.)

$\langle -1-12\rangle$. In Fig. 9(a), the most intense and sharp double peaks are $K_{\alpha 1}$ and $K_{\alpha 2}$ of the Si (*hkl*) ($h = k = l = 1, 2, 3$) reflections. The hex-$Pr_2O_3(000n)$ and cub-$Pr_2O_3(nnn)$ ($n = 2, 4, 6$) Bragg peaks arise at the right and left side of Si(*hkl*) reflections. Further quantitative analysis shows that CeO_2 on hex-Pr_2O_3 layers is almost entirely relaxed whereas CeO_2 on cub-Pr_2O_3 layers is still partly tensily strained. Fig. 9(b) displays the SR-GIXRD scan along the $[01l]_S$ rod allowing a precise stacking twin analysis because the oxide peaks and Si peaks are not overlapping. It can be observed that hex-Pr_2O_3 reflections $(01-1n)$ are located at $l = 0.517n$ r.l.u. ($n = 1, 2, 3, \ldots$). Strong (1−11) and (202) reflections of type-B CeO_2 are detected at $l = 0.335$ and 1.340 r.l.u., respectively; and no type-A oriented $CeO_2(111)$ domains are found within the detection limit, considering that the allowed type-A $CeO_2(020)$ reflection is not visible with more than 0.01% intensity ($I_{0.01\%}$) of the $CeO_2(002)$ maximum intensity (I_{max}).

As the type-B oriented growth of $CeO_2(111)$ on a hex-Pr_2O_3/Si(111) support appears to be surprising considering the stacking sequence transition from ACACAC… to ABCABC… at the $CeO_2(111)$/hex-$Pr_2O_3(0001)$ interface, *ab initio* calculations have

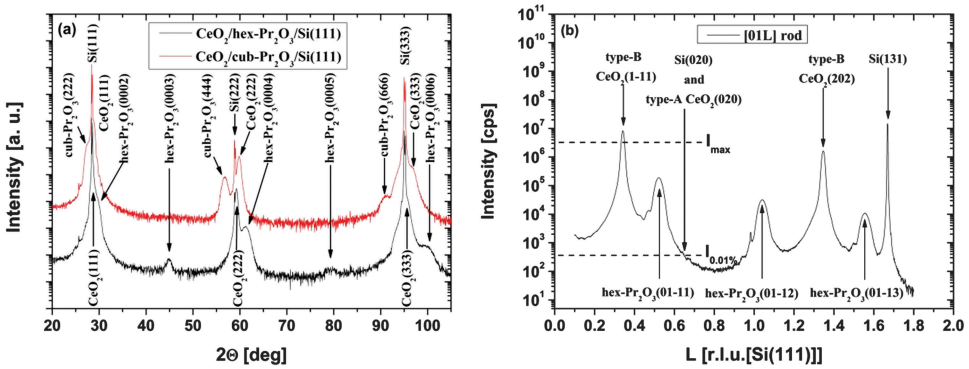

Fig. 9 (a) Specular XRD θ–2θ measurements for a 38 nm thick CeO_2/hex-Pr_2O_3/Si(111) and a 22 nm thick CeO_2/cub-Pr_2O_3/Si(111) heterostructure. (b) SR-GIXRD scan along the $[01l]_S$ rod of the CeO_2/hex-Pr_2O_3/Si(111) sample. (Reproduced from ref. 74.)

been performed to identify the microscopic origin of this behaviour.[26] The model of Fig. 10(a) shows that two facts are responsible for the preference of the type-B orientation. (i) The formation of a Pr^{4+} monolayer conserves the semiconducting character of the CeO_2/Pr_2O_3 interface and leads to an electronic continuation. (ii) The oxygen sub-lattice transports a BACBAC stacking information and keeps the crystallographic continuation. In contrast, type-A oriented $CeO_2(111)$ would cause a stacking fault at the interface. Thus, type-B oriented $CeO_2(111)$ on hex-$Pr_2O_3(0001)$/Si(111) is favoured by 8 eV nm^{-2}.[74] HRTEM cross-sectional images shown in Fig. 10(b) and (c) exhibit the details of a CeO_2 layer on hex-Pr_2O_3 and cub-Pr_2O_3 buffers, respectively. Notably, interfacial layers are formed even in a CeO_2/hex-Pr_2O_3/Si heterostructure.

III 1.3 Mixed $Ce_{1-x}Pr_xO_{2-\delta}$ oxide films. While the bilayer CeO_2/Pr_2O_3 heterostructures are interesting for the observation of oxygen exchange at the oxide interface, the mixed $Ce_{1-x}Pr_xO_{2-\delta}$ oxide films offer further possibilities such as lattice parameter engineering and tailoring oxygen vacancy structures (see Section III.2.6). The stoichiometry and valence states of such films are studied by *in situ* XPS (not shown here), indicating that with increasing Pr^{3+} doping, the Ce^{3+} valence state is more stabilised.[113] An extensive XRD study allows an identification of the film structure as a function of the stoichiometry. Fig. 11(a) shows specular θ–2θ XRD measurements on mixed $Ce_{1-x}Pr_xO_{2-\delta}$ films with x = 0.3, 0.7 and 0.8. Evidently, when $x \leq 0.7$, with higher x values (higher Pr^{3+} concentration), the mixed oxide Bragg peak moves to smaller 2θ angles, corresponding to a lattice expansion. This is consistent with the prediction of Vegard's law,[114] as shown in Fig. 11(d) showing the bulk lattice parameter variation as a function of the Pr concentration determined by XRD. This confirms the XRD study on mixed $Ce_{1-x}Pr_xO_{2-\delta}$ powder performed by McCullough *et al.*[115] Furthermore, SR-GIXRD measurements along the $[h00]_S$ direction on x = 0.3 and 0.7 samples are performed to reveal the lattice details in the mixed oxides, as shown in Fig. 11(b). The upper panel shows the results for the x = 0.3 sample with only a single peak close to the position h = 3 arising that belongs to the fluorite lattice (22−4) Bragg reflection. However, with increasing Pr^{3+} doping (x = 0.7), the lattice is distorted in favour of the bixbyite lattice. Therefore, in the lower panel an additional peak appears at h = 2.25 that is related to the bixbyite lattice (33−6) Bragg reflection. However, it is still not clear if there exist fluorite phases in the mixed oxides that are dominated by the bixbyite structure. For higher Pr^{3+}doping (x = 0.8), a pure Ce^{3+} valence state is stabilised, forming a hexagonal crystal structure, as seen in the XRD pole figure results shown in Fig. 11(c). This measurement was taken at $2\theta = 56.5^\circ$ on a $Ce_{0.2}Pr_{0.8}O_{2-\delta}$/Si(111) sample. Here, we detect the 6-fold symmetry of the purely hexagonal structure ({02−21} reflections) of the film (open circles, $\chi = 75^\circ$

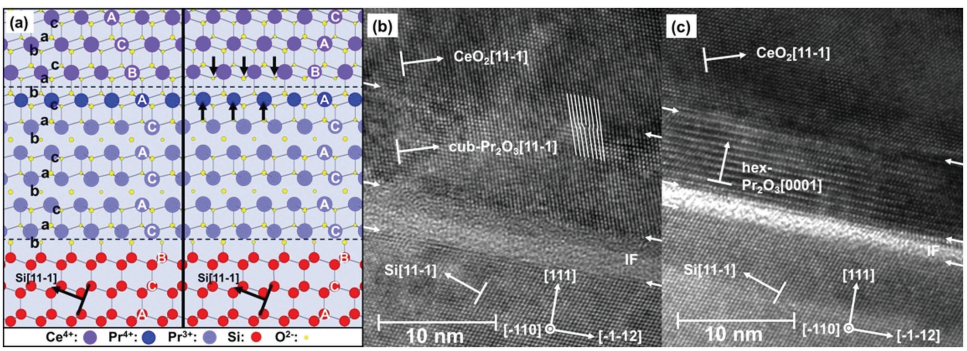

Fig. 10 (a) Atomistic interface model for type-A and -B $CeO_2(111)$/hex-$Pr_2O_3(0001)$/Si(111) layer stacking. (b) HRTEM image of the cub-$Pr_2O_3(111)$/Si(111) interface. (c) HRTEM image of the hex-$Pr_2O_3(0001)$/Si(111) interface. (Reproduced from ref. 26.)

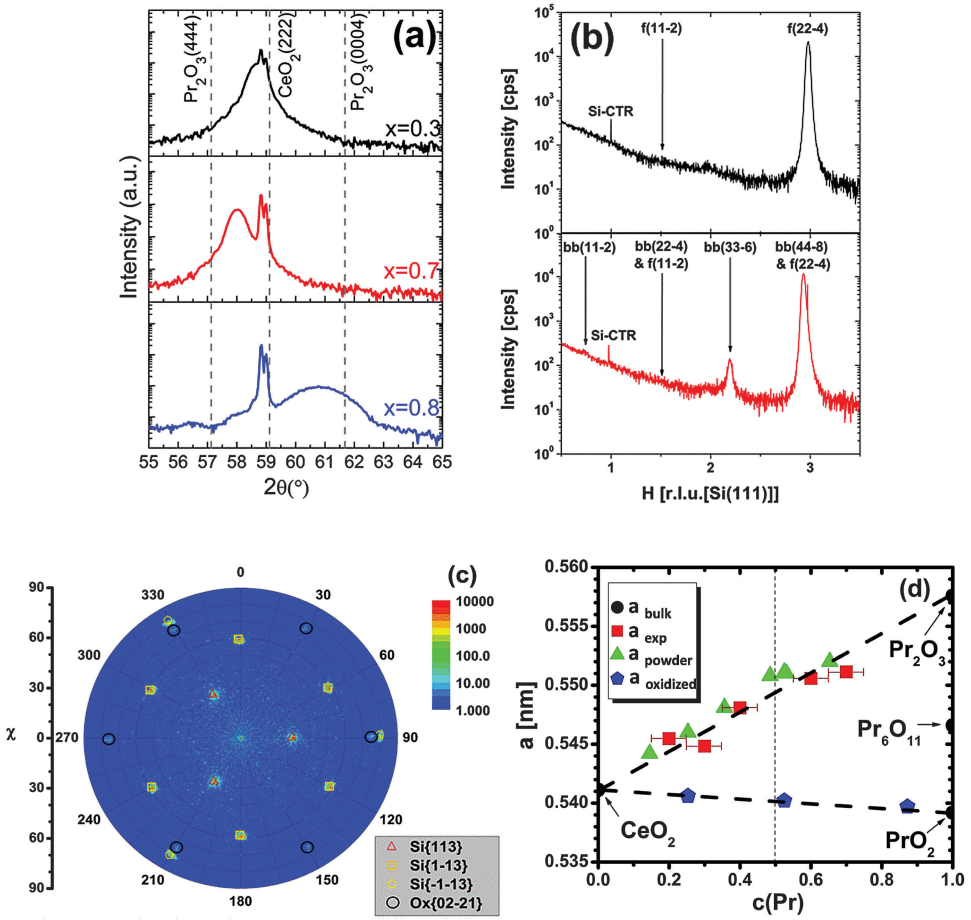

Fig. 11 (a) Specular θ–2θ XRD measurements of 24 nm thick $Ce_{1-x}Pr_xO_{2-\delta}$/Si(111) samples (x = 0.3, 0.7, 0.8). The dotted straight lines mark the Bragg peak positions of cubic Pr_2O_3(444), CeO_2(222) and hexagonal Pr_2O_3(0004), respectively. (b) GIXRD scan along the $[H00]_S$ direction of $Ce_{0.7}Pr_{0.3}O_{2-\delta}$ and $Ce_{0.3}Pr_{0.7}O_{2-\delta}$ films (f: fluorite structure, bb: bixbyite structure). The Pr-rich sample exhibits an additional bixbyite phase as evident from the bb(33–6) peak. (c) Pole figure measurement of $Ce_{0.2}Pr_{0.8}O_{2-\delta}$(0001)/Si(111) measured at 2θ = 56.5 °. Black circles demonstrate the six-fold symmetry and thus a hexagonal crystal structure. (d) The bulk lattice parameter variation of the films as a function of the Pr concentration in the films. The reference from powder studies[21,115] is given for comparison. (Reproduced from ref. 113.)

where χ is the angle between the oxide lattice planes and the Si substrate normal[116]). All other spots in the pole figure are related to Si reflections. To further clarify the phase transition with Pr doping into the CeO_2 lattice from a microscopic point of view, SR-XAFS measurements on similar samples are performed and it is found that, with increasing Pr concentration in CeO_2, the local lattice distortion gradually increases.[117] Distinguishing between cub- and hex-ternary $Ce_{1-x}Pr_xO_{2-\delta}$ mixed oxide thin films, one can find the epitaxial relationships cub-$Ce_{1-x}Pr_xO_{2-\delta}$(111); $\langle 11{-}2\rangle \| Si(111)$; $\langle -1{-}12\rangle$ for x = 0.2–0.7 and hex-$Ce_{1-x}Pr_xO_{2-\delta}$(0001); $\langle -1100\rangle \| Si(111)$; $\langle -1{-}12\rangle$ for x = 0.8.

We note here that due to the valence state difference between Pr^{3+} and Ce^{4+}, the doping of Pr into the CeO_2 lattice is an effective way to induce oxygen vacancies $V_O^{\bullet\bullet}$ in CeO_2 films. It is well known that oxygen vacancies can strongly affect physical and chemical properties of oxides, such as the conductivity, optical and catalytic properties. For example, recently it has been reported that the room temperature ferromagnetism (RTFM) in diluted magnetic oxides is strongly related to oxygen vacancies[118,119] and our $Ce_{0.8}Pr_{0.2}O_{2-\delta}$ film shows strong magnetic properties.[120] The oxidative reactivity as a function of the Ce–Pr stoichiometry within different gas ambiances like CO, H_2O and O_2 is introduced in Section III.2.6.

III.2 Surface structure and morphology

The surface structure of praseodymia films as well as of ceria films has been studied by the high resolution diffraction of low energy electrons to obtain a better insight into their symmetry properties. Furthermore, the surface morphology has been studied analysing the profiles of diffraction peaks to explore the diversity of the film systems.

III.2.1 Surface structure of pure praseodymia phases. Surface investigations on hexagonal Pr_2O_3(0001) films are challenging due to their instability under ambient conditions that stems from $Pr(OH)_3$ formation.[121,122] The hydroxide exhibits a hexagonal structure similar to hex-Pr_2O_3 and, therefore, hydrogen is easily incorporated in hex-Pr_2O_3 without major changes in the crystalline structure; the entire film is transformed to $Pr(OH)_3$ after a relatively short time of exposure under ambient conditions. For this reason, capping layers are needed to transport hexagonal

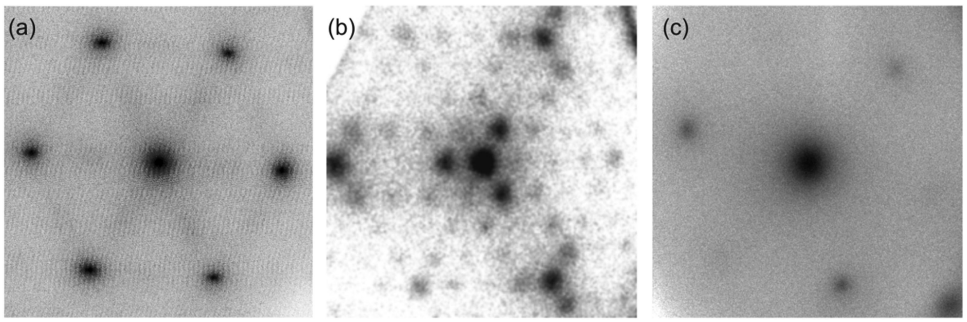

Fig. 12 2D high resolution electron diffraction patterns of praseodymia film surfaces; (a) for a 9 nm thick hex-Pr_2O_3(0001), (b) for a 9 nm thick cub-Pr_2O_3(111) and (c) for a 12 nm PrO_2(111) film. (Reproduced from ref. 123 and 124.)

Pr_2O_3 films. Our studies reveal that amorphous germanium is a feasible capping layer since it can be removed by annealing in a diluted oxygen atmosphere without changing the structure of the underlying hex-Pr_2O_3(0001) film as shown by combined AES and GIXRD measurements.[123] Furthermore, high resolution SPA-LEED measurements of the hex-Pr_2O_3(0001) surface exhibit a hexagonal (1 × 1) diffraction pattern with obviously no intensity variations of the first order diffraction spots as seen in Fig. 12(a) while a threefold symmetry is observed for (111) surfaces of films with a bulk cubic structure as (seen in Fig. 12(b) and (c)). This effect is caused by the small but finite penetration depth of low energy electrons. The six-fold intensity symmetry points to ABABAB... stacking for the hex-Pr_2O_3(0001) film while the threefold symmetry is caused by a cubic ABCABC... stacking.

For cubic Pr_2O_3, hydroxide formation is limited to the topmost layers of the film.[95] If transported under ambient conditions, the majority of the bulk structure is preserved and only minor oxidation occurs as shown by XRD.[124] It is further found that a clean single phase Pr_2O_3(111) film can be prepared by annealing the cub-Pr_2O_3(111) at temperatures above 300 °C under UHV conditions to remove hydroxides from the surface.[124] Therefore, we assume that a hydroxide layer as well as the excess oxygen can be removed by annealing at higher temperatures and no capping layer is needed to transport cub-Pr_2O_3(111) film under ambient conditions. The SPA-LEED measurements of the cub-Pr_2O_3(111) film shown in Fig. 12(b) exhibit a hexagonal (4 × 4) diffraction pattern. This pattern is attributed to the bixbyite structure of (111) oriented Pr_2O_3 having a 16 times larger surface unit cell than hex-Pr_2O_3. In addition, a three-fold symmetry of the first order diffraction spot intensities clearly appears due to the ABCABC... stacking of the cubic structure.

Contamination free cub-PrO_2(111) surfaces can be prepared by plasma oxidation of cubic $PrO_{2-\delta}$(111) films.[94] SPA-LEED measurements of such films show a hexagonal (1 × 1) diffraction pattern due to the (111) orientation of the cubic fluorite type unit cell. As shown in Fig. 12(c), the intensity of the first order diffraction spots exhibit the same threefold symmetry based on the ABCABC... stacking as observed for the cub-Pr_2O_3(111) film.

III.2.2 Surface structure of pure ceria phases. In contrast to praseodymia, a hexagonal Ce_2O_3 phase cannot be stabilised on Si(111) if a ceria evaporation source is used since ceria crystallises in the highest oxidation state as cub-CeO_2(111). Hence, reduced ceria phases can only be obtained by the reduction of the initial CeO_2(111) film. For ceria films of 250 nm thickness, the cub-Ce_2O_3(111) surface is prepared by annealing in UHV at ~1150 K for 30 minutes.[97] Since cub-Ce_2O_3 exhibits the same bixbyite structure as cub-Pr_2O_3(111), a similar hexagonal (4 × 4) LEED pattern is observed as for cub-Pr_2O_3(111) (Ce_2O_3 not shown, Pr_2O_3 shown in Fig. 12(b)). However, the overall intensity of all diffraction spots is reduced in comparison to cub-Pr_2O_3(111) indicating a higher density of point defects at the surface. After oxygen plasma cleaning,[97] the surface structure of CeO_2(111) is similar to the one of PrO_2(111) since both crystals exhibit the same fluorite type crystal structure.

III.2.3 Surface morphology of pure praseodymia phases. The surface morphology of hex-Pr_2O_3(0001) is determined by a spot profile analysis of the central diffraction spot of the LEED pattern recorded at different electron energies. The spot profile is fitted with two Lorentzian functions as illustrated in Fig. 13. The first Lorentzian describes the contributions of atomic surface steps leading to an oscillating full width at half maximum (FWHM) for changing electron energies while the second broader Lorentzian accounts for small surface inhomogeneities, resulting in a constant FWHM independent of the electron energy. From the analysis of the oscillating function, the surface morphology of the hex-Pr_2O_3(0001) film is deduced.[123] The surface consists of small grains (~1.7 nm) but is very smooth since only few grains exhibit single atomic steps of full unit cell height as indicated in the model presented in Fig. 15. We conclude that a large amount of smooth grains without steps is present at the surface where the small surface roughness is a result of the high quality epitaxial growth of the hex-Pr_2O_3(0001) film (Fig. 14).

The SPA-LEED analysis of single phased cub-Pr_2O_3(111) also shows an oscillating FWHM of the specular diffraction peak due to single atomic steps at the surface as shown in Fig. 16. The average terrace size on cub-Pr_2O_3(111) is, however, significantly smaller than that for hex-Pr_2O_3(0001) and the density of atomic steps is significantly larger.[95] Furthermore, in contrast to hex-Pr_2O_3(0001) films, a mosaic spread is concluded from an additional linear increase of the FWHM with increasing electron energy indicating a higher overall roughness of the surface. We assume that the surface roughening originates

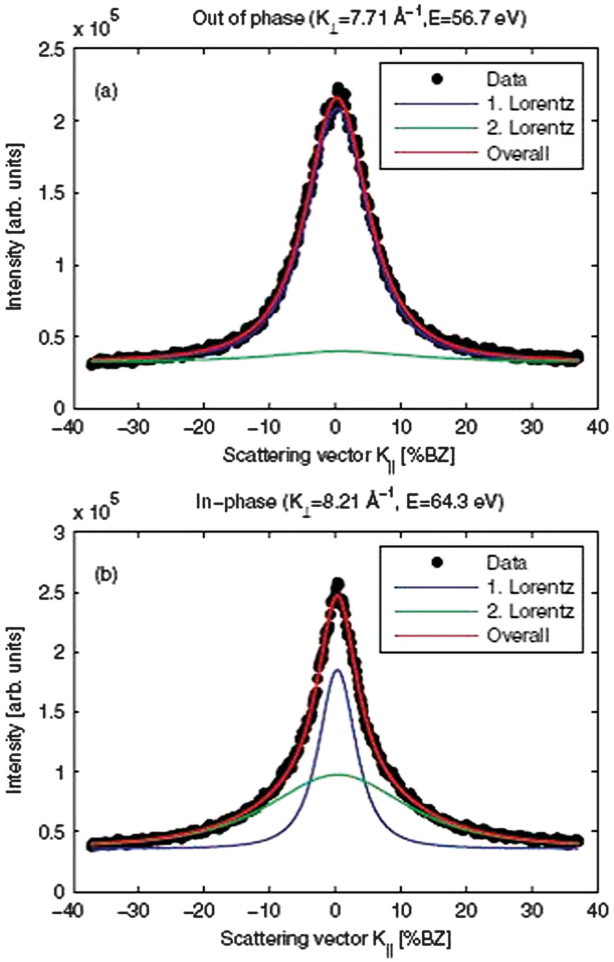

Fig. 13 Cross-section of the central diffraction spot for a 9 nm thick hex-Pr_2O_3(0001) film for (a) anti-Bragg conditions (out-of-phase) and (b) Bragg conditions (in-phase). Two Lorentzian functions are necessary to describe the spot profile. (Reproduced from ref. 123.)

from strain effects induced during the hex-to-cub transition. The stress is caused by the lateral pinning of the oxide film to the lattice of hex-Pr_2O_3(0001) at the Si interface causing a strong vertical distortion of the cub-Pr_2O_3(111) film.[92] Thus the film partly releases the high compressive stress *via* the formation of tilt mosaics as sketched in Fig. 15(b).

To confirm and elaborate on the spot profile analysis results, the surface morphology of cub-Pr_2O_3(0001) films as grown and after annealing is investigated by NC-AFM under UHV conditions[125] allowing for direct imaging of surface topographic features and a detailed analysis of the origins of roughness. Experimental methods for sample preparation, NC-AFM imaging and the instrument used have been described in detail elsewhere.[26,27,126,127] Fig. 17 shows a comparison of imaging results for films with 10, 50, 100 and 200 nm thickness for surfaces prepared by post-deposition annealing for one hour at 830 K. This annealing temperature is chosen because it causes no significant change in the surface morphology compared to non-prepared samples but removes some contaminants present due to the transport of the sample under ambient conditions.

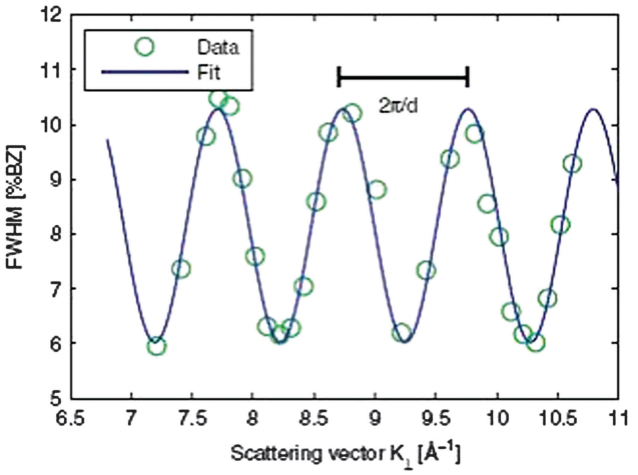

Fig. 14 The FWHM of the central diffraction spot for a 9 nm thick hex-Pr_2O_3(0001) film oscillates with increasing scattering vector $K_\perp$ perpendicular to the surface indicating single atomic step heights. By modelling the oscillation with a cosine function, the average step height d and terrace width can be determined. The additional constant offset of the FWHM is attributed to small grain sizes. (Reproduced from ref. 123.)

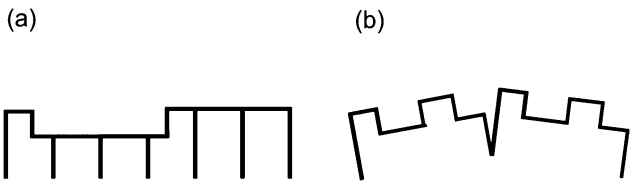

Fig. 15 Schematic model of the hex-Pr_2O_3 (a) and cub-Pr_2O_3 (b) surface morphology.

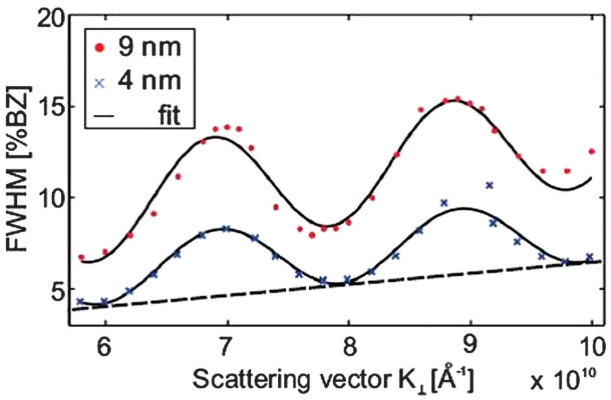

Fig. 16 FWHM of the central diffraction spot against scattering vector $K_\perp$ for cub-Pr_2O_3(111) films of different thicknesses. Similar to the hex-Pr_2O_3(0001) films, an oscillating behaviour due to single atomic steps is observed. The step height and terrace width can be determined by fitting a cosine function superimposed by a linear function to the data. The linear contribution is caused by the mosaic spread of the cub-Pr_2O_3(111) films. (Reproduced from ref. 124.)

The frame size of 250 nm × 250 nm allows for an identification of individual surface features but also for an assessment of the roughness at different scales and the overall homogeneity. The surface morphology significantly varies with film thickness.

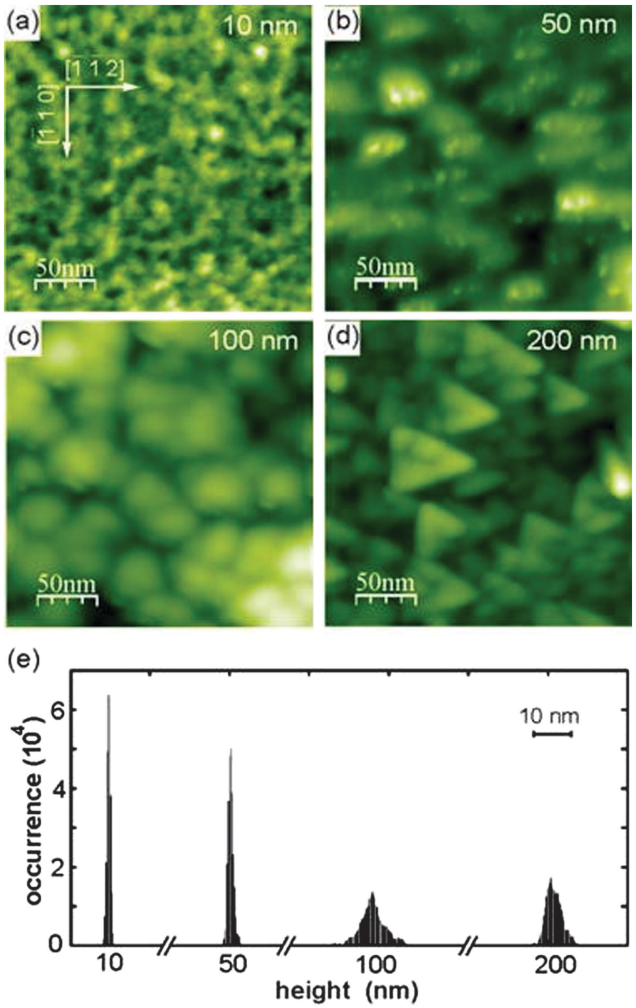

Fig. 17 (a) to (d) NC-AFM images representing the topography of cub-Pr_2O_3(0001) films with a thickness of (a) 10 nm, (b) 50 nm, (c) 100 nm and (d) 200 nm after post deposition annealing to 830 K. The in-plane crystallographic directions denoted in (a) are the same for all images. (e) The height distribution illustrates a significant difference in roughness between thinner and thicker films. The quantity plotted along the ordinate represents the number of image pixels from the 512 × 512 total pixels having a height within an interval of 0.33 nm around the value plotted along the abscissa. The width of the distributions are a measure for the RMS surface roughness.

On the surface of the 10 nm film shown in Fig. 17(a), no well-shaped features are found and the height of the irregular structures present is in the range of 2 to 3 nm. The 50 nm film shown in Fig. 17(b) reveals more contiguous, slightly rounded features where some of them appear with a triangular shape. Height differences on the surface are larger compared to the 10 nm film, however, overall the surface is relatively flat. This can also be deduced for the roughness analysis shown in Fig. 17(e) where the 10 and 50 nm films appear with a rather narrow height distribution. For the 100 nm film shown in Fig. 17(c), the surface is dominated by roundish features with a typical size of 30 nm. In contrast to the thinner films, the surface is rough on a 10 nm lateral scale. With height differences amounting to several nanometres, this sample has a roughness that is by a factor of five larger than the roughness of the 50 nm film. The 200 nm film shown in Fig. 17(d), in contrast, reveals oriented triangular islands with rather straight edges where the vertices of the triangles point into [−1−12] directions. The surface roughness is comparable to the roughness of the 100 nm film. The trend in roughness can be explained by a phenomenon commonly referred to as kinetic roughening.[128,129] The first layers of the film are grown in a two-dimensional mode resulting in a rather flat surface. Then the growth mode changes to a three-dimensional mode for increasing thickness where the growth of the next layers starts before the first layer is completed. This leads to the formation of islands and surface roughening. Note, however, that numerical values for the roughness of differently thick films cannot easily be compared with each other as the surface morphology changes with film thickness.

The results of a measurement on a larger scale after annealing the 200 nm film for one hour at 570 K are presented in Fig. 18(a). The image is dominated by triangular islands often having a 10 nm wide rim with an opening at one side as is best seen in the three-dimensional representation of an island shown in Fig. 18(b). Triangular islands have a side length of 50 to 60 nm and a height in the range of 6 to 10 nm where the side facets have a slope of approximately 30°. While we speculate that the rim formation is related to peculiarities of the growth in a fluorite type lattice,[130] the formation of pyramids with a triangular base is discussed below in the context of ceria film growth in Section III.2.4. Attempts for obtaining a better ordered and cleaner film surface by annealing the film at higher temperature to allow for imaging with higher resolution fail as the film decomposes when annealed at temperatures higher than 850 K as demonstrated in Section III.2.5.1.

In summary, we note that the surface of the cub-Pr_2O_3(0001) film exhibits characteristic structural features where the morphology of the thickest films investigated is dominated by regular and oriented triangular islands with a surface appearing rather flat. Annealing at higher temperatures yields a cleaner surface and slight changes in detail; however, the nanoscale surface morphology does not change during annealing at temperatures up to 830 K defining the limit for the decomposition of the film. The as-grown film visually appears with different shadings of red and violet depending on film thickness and preparation details as shown in the example of Fig. 18(c). The colour changes to grey upon heating beyond the decomposition limit of 830 K as seen in Fig. 18(d). When the as-grown film is treated in an oxygen plasma as described in Section II.2, the surface morphology does not change (see Fig. 18(e)), however, the colour changes to green as shown in Fig. 18(f) and back to violet upon heating the plasma-treated sample to a temperature of 630 K (the results not shown).

III.2.4 Surface morphology of pure ceria phases. Similar to the praseodymia phases, SPA-LEED is performed for cub-Ce_2O_3(111) and cub-CeO_2(111) films[97] as shown in Fig. 19. In contrast to cub-Pr_2O_3(111) films, no oscillating behaviour of the spot profile is observed for the cub-Ce_2O_3(111) phase indicating very large terraces. Furthermore, the low peak to background ratio for the diffraction pattern indicates a large amount of point defects. On the other hand, the FWHM of the specular

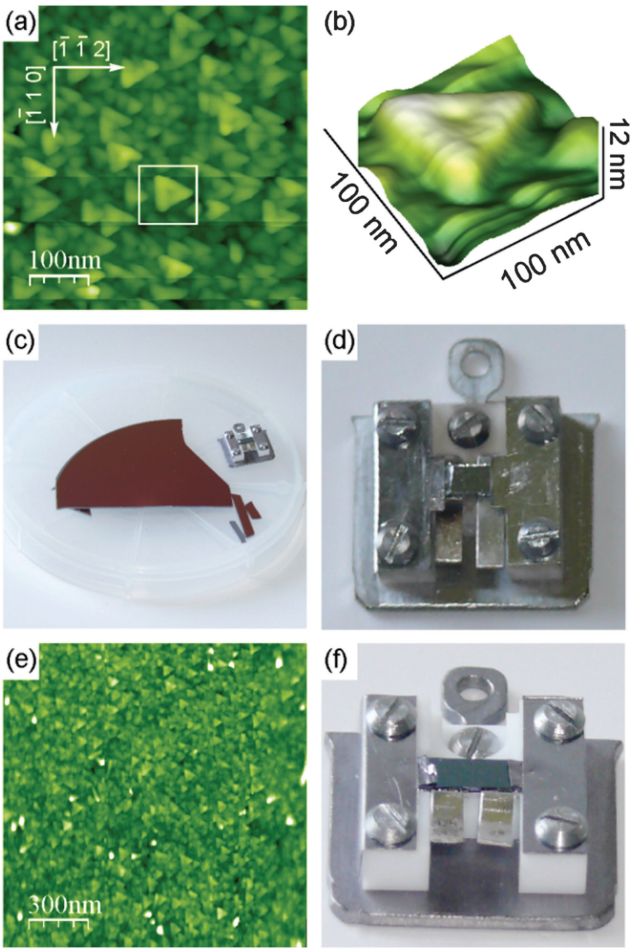

Fig. 18 (a) Topography of a 200 nm thick cub-Pr_2O_3(0001) film exhibiting a morphology dominated by triangular islands oriented in the [−1−12] direction. The orientation of the film is the same as in Fig. 17. (b) Three-dimensional representation of the island marked in (a) revealing the 10 nm wide rim with an opening terminating the island. (c) Photo of the as-prepared sample with the film exhibiting a red/violet colour. (d) Photo of the sample holder with the sample after annealing at a temperature above 850 K yielding a grey colour. (e) Topography of a 200 nm thick cub-Pr_2O_3(0001) film subjected to oxygen plasma treatment. (f) Photo of the sample holder with the sample after plasma treatment of the as-grown sample yielding a green colour.

(00) diffraction spot of cub-CeO_2(111) films seen in Fig. 19(b) exhibits a behaviour similar to the one of the cub-Pr_2O_3(111) seen in Fig. 16. Single atomic steps with a height of the layer spacing of CeO_2(111) are present at the surface. In addition, the surface shows a mosaic spread. The average terrace width of about 6 nm is larger than for praseodymia films.

To reveal the structure of the facets in detail, NC-AFM imaging is performed on surfaces of as-prepared and slightly heated cub-CeO_2(111) samples[131] using instruments and methods described earlier.[23,26,27,127] Here, we discuss the morphology for the as-prepared and slightly heated 180 nm cub-CeO_2(111) film that will further on be denoted as the low temperature morphology. In this temperature regime, post-deposition preparation does not affect the film surface structure significantly; however, the film is slightly reduced as will be discussed in Section III.2.5.2. The NC-AFM image shown in Fig. 20(a) represents a result for the as-prepared film while the results for a film heated to 510 K is shown in Fig. 20(b). Annealing the film to 510 K removes parts of the contamination layer on the sample surface, thus, allowing for imaging more structural details on the surface. The images exhibit a distinct surface structure consisting of large triangular based, oriented pyramidal islands that are 4 to 6 nm high and have an edge length of typically 100 nm. Close inspection reveals a terrace structure forming the pyramids as most clearly seen in Fig. 20(c). Pyramidal faces are composed of 3 to 5 nm wide (111) terraces separated by step edges with a height of 0.31 nm corresponding to the height of one O–Ce–O triple layer in agreement with the SPA-LEED results introduced above. The average slope of the pyramidal facets is determined by a cross-sectional analysis performed on several pyramids. The analysis yields different slopes for the bottom and top layers of the pyramids. For the bottom layers, we find a slope angle of 10° relative to the (111) surface plane which can be associated with a {332} facet while the top layers exhibit an angle of 5° relative to the (111) surface plane that can be associated with a {665} facet. Fig. 20(d) represents a side view model of the two facets yielding slope angles and terrace widths in good agreement with experimental observations. This analysis shows that the as-grown cub-CeO_2(111) film provides a ceria surface exhibiting an exceptionally rich structure of step edges regularly arranged in terraced pyramids. Such a film could be most interesting for applications requiring a large number of regular steps with a height of one O–Ce–O triple layer.

Beyond possible applications of the ceria film, it is interesting to discuss the growth mechanism yielding the pyramidal island structure. As a hypothesis, we anticipate that the nucleation of CeO_2 is templated by the praseodymia buffer layer grown in a well-defined orientation and registry on the Si(111) substrate (see Section III.1.2). We further assume that the growth of the pyramidal structures is due to a kinetically limited process, similar to the one proposed for the homoepitaxial growth of platinum on Pt(111).[132] As ceria crystallises in the fluorite structure, two different types of step edges, namely type-A and type-B, are relevant for a growth process on the (111) surface.[23,133] The probability for particle attachment is higher at steps of type-A so that type-B steps grow faster and preferentially triangles are grown, although, the substrate exhibits a hexagonal surface symmetry.[130] The pyramidal structures are commonly referred to as wedding cakes that are the result of a multilayer growth in the presence of a significant Ehrlich–Schwoebel barrier.[134–136] Adatoms that adsorb during MBE on the top of a terrace diffuse to the borders if enough thermal excitation energy is available. In the absence of a step edge barrier, the adatoms would easily overcome the ascending step edge at the border and diffuse to a lower terrace finally resulting in the growth of a flat surface. However, if an Ehrlich–Schwoebel barrier is present and larger than the average diffusion energy, the adatoms cannot overcome step edges easily. While the probability for diffusion of adatoms to lower terraces is reduced, the probability for building a new layer by the remaining adatoms increases.

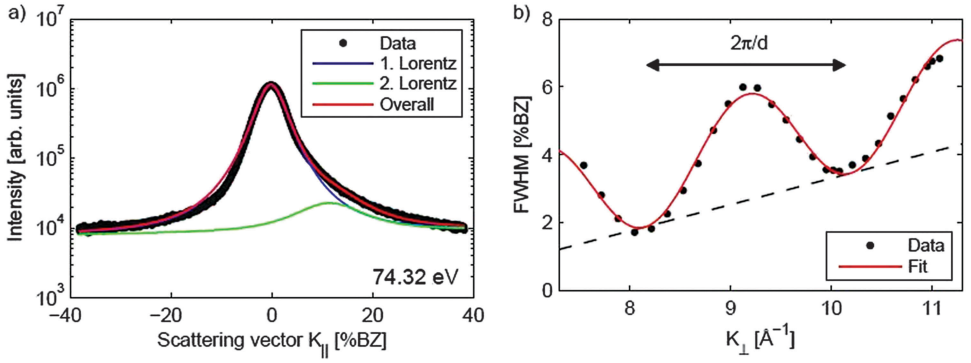

Fig. 19 (a) Spot profile of the specular (00) diffraction spot of a 250 nm thick CeO_2(111) film. The asymmetric peak shape is caused by surface facets, thus, two functions are needed to describe the spot profile. (b) FWHM of the central peak plotted against the scattering vector $K_\perp$. Similar to observations for a praseodymia film, single atomic steps are present at the surface resulting in an oscillation of the FWHM. In addition, a linear increase of the FWHM due to mosaics is observed. (Reproduced from ref. 97.)

This results in an enhanced intra-layer diffusion on the cost of inter-layer diffusion and the synchronous growth of structures on all terrace levels. The change in the slope between the bottom and top layers is attributed to a change in the Ehrlich–Schwoebel barrier during the growth process.

III.2.5 Surface morphology: phase transitions due to film reduction

III.2.5.1 Reducing PrO_2. The reduction behaviour of PrO_2(111) films has been the subject of several detailed studies.[94,96,107,137] As discussed in Section II.1, XPS measurements reveal that fully oxidised PrO_2(111) films can only be achieved by oxygen plasma treatment.[94] The Pr 3d spectra shown in Fig. 21 exhibit a complex peak structure based on hybridization between the Pr 4f states and the O 2p valence band. However, the amount of Pr^{4+} ions can be estimated by the relative intensity of the peak labelled as z (or z'). By thermally reducing the film, it can be observed that the intensity of the z (or z') peak is lowered. Thus, the Pr^{4+} concentration is decreased revealing a homogeneous reduction of the film surface.

The loss of oxygen has also been confirmed by TPD experiments. Characteristic peaks can be observed in the TPD spectra of molecular oxygen shown in Fig. 22 suggesting thermally induced phase transitions.[94,107] However, the corresponding XRD analysis of the PrO_x(222) Bragg peak reveals that these transitions result in coexisting oxide phases of different stoichiometries as evident from the appearance of coexisting praseodymia Bragg peaks in XRD measurements shown in Fig. 23.

It was further shown by out-of-plane GIXRD measurements that praseodymia films are pinned to the lateral lattice constant of hex-Pr_2O_3(0001) and, thus, tetragonally distorted during film growth.[92] This growth induced exclusive pinning of the lateral lattice constant is breached during the reduction process. An explanation for the de-pinning is the transformation to an amorphous interface between the substrate and film at elevated temperatures.[137] The stoichiometries of the coexisting oxide phases are determined by a calculation of their pseudo-cubic lattice constants from the in-plane and out-of-plane GIXRD data for the tetragonally distorted film with the results shown in Fig. 24.[107] All intermediate phases of praseodymia are formed by vacancy generation in the oxygen sublattice of the fluorite structure of PrO_2 and, thus, these vacancies result in an expansion of the cubic unit cell due to the decreased average oxidation state of praseodymium. Following Vegard's law,[114] the film stoichiometry can be determined. Thus, the expansion of the re-calculated bulk lattice constant is directly proportional to the stoichiometry of the corresponding intermediate phase.

In summary, we find that PrO_2 films are not homogenously reduced.[96,107,137] Combining the results from the surface sensitive SPA-LEED measurements with an analysis of XRD results, a structure model for the reduction process is developed as depicted in Fig. 7. During the reduction, a mosaic spread is formed at the surface[92,137] while the amorphisation of the interface layer underneath the coexisting oxide phases progresses during heat treatment.

III.2.5.2 Reducing CeO_2. The reduction properties of CeO_2(111) films show similarities but also significant differences in comparison to PrO_2(111) films. For instance, after annealing at 600 °C, praseodymia films are fully reduced to cub-Pr_2O_3(111)[124] while ceria films exhibit only slight oxygen loss at the surface as shown by XPS while the bulk does not change its stoichiometry as evident from the XRD results shown in Fig. 25 and 26, respectively.[97] As a similarity we find that also ceria films like praseodymia films form coexisting phases when annealed under UHV conditions. After annealing at 650 °C, the Ce_7O_{12} phase is stabilised which can also be detected at the surface of the film.[138] The non-uniform reduction of ceria is concluded from the $CeO_2(111)_B$ bulk diffraction peak that is present even after the formation of the Ce_7O_{12} phase. As evident from Fig. 26, further annealing at 700 °C leads to the additional stabilisation of the $Ce_{11}O_{20}$ phase having a higher oxygen content than the coexisting Ce_7O_{12} phase. Since no increase of the oxygen content is observed at the surface as evident from Fig. 25, we assume that $Ce_{11}O_{20}$ is formed close to the interface between the substrate and film due to oxygen diffusion towards the substrate. In contrast to praseodymia, single phased cub-Ce_2O_3(111) films cannot be prepared by annealing in UHV. The high temperatures needed to form cub-Ce_2O_3(111) for the entire film destroy the

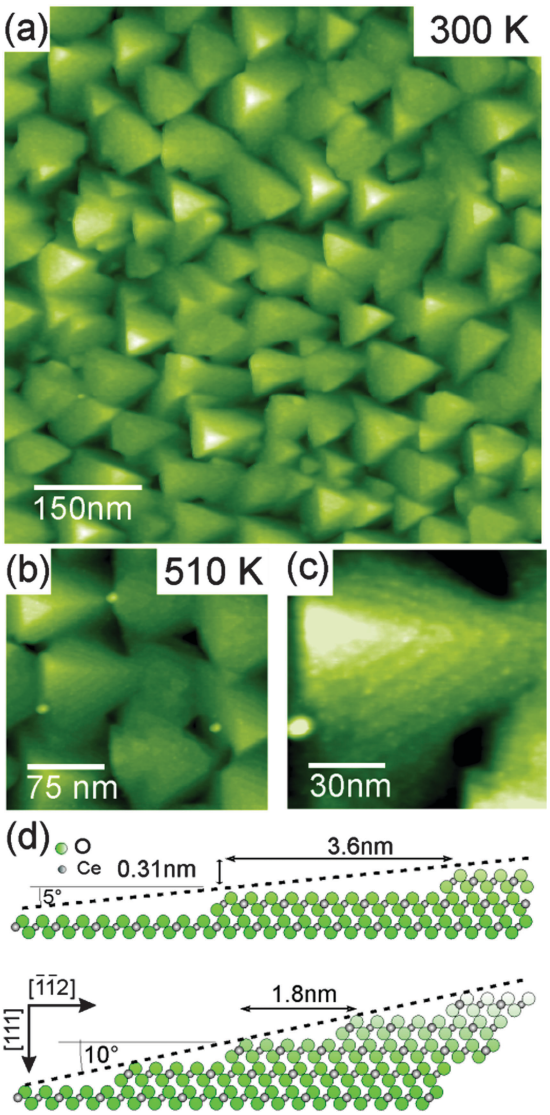

Fig. 20 (a) to (c) NC-AFM images taken on a cub-CeO_2(111) sample representing (a) the as-prepared ceria sample and (b and c) the sample heated to a temperature of 510 K. The terrace structure of the pyramid is clearly seen in (c). Bright spots preferentially attached to step edges are due to contaminants that could not be removed by the heat treatment. (d) Side view model for the bottom (typically 10) and top (typically 5) layers of the pyramids yielding nominal values for the terrace widths and slope angles. (Reproduced from ref. 131.)

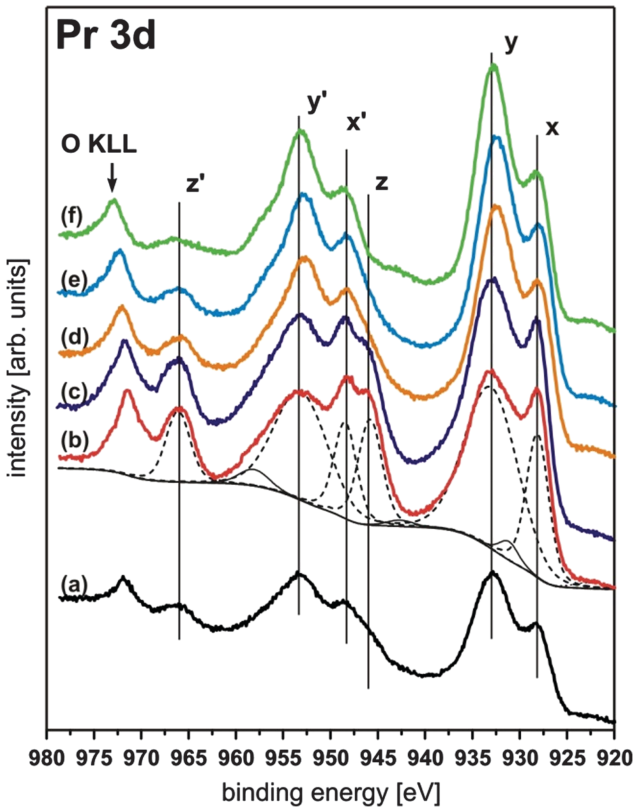

Fig. 21 Pr 3d XP spectra of a 15 nm thick PrO_2(111) film composed of three peaks (x, y, z) in each $3d_{5/2}$ and $3d_{3/2}$ component. The peaks labelled with z and z' are directly related to the amount of Pr^{4+} ions present at the surface. Hence, the intensity of the z and z' peaks drastically increases after the as-prepared $PrO_{2-\delta}$ sample (a) is exposed to an oxygen plasma yielding a contamination free PrO_2 surface (b). Subsequent annealing under UHV conditions (405 K (c), 580 K (d), 680 K (e), and 920 K (f)) leads to a reduction of the films as shown by the decreasing intensity of the z or z' peak. (Reproduced from ref. 94.)

film by the formation of silicides and silicates.[97,131] However, careful UHV annealing close to 880 °C forms cub-Ce_2O_3(111) in the near-surface region as proved by SPA-LEED measurements (not shown) and XPS results shown in Fig. 25.

As in the case of praseodymia (see Section III.2.5.1), the nanoscale surface structure of a ceria film is not influenced by its reduction. However, a detailed NC-AFM study reveals a dramatic change in surface morphology upon annealing the film.[131] The as-prepared surface exhibits a metastable structure that is denoted as the low temperature morphology being stable against annealing at temperatures up to 850 K. A distinctly different morphology, referred to as the high temperature morphology, is found in the temperature range of 930 K to 1100 K where Ce_7O_{12}, $Ce_{11}O_{20}$ and Ce_2O_3 stoichiometries are present.

The basic surface structures of the as-prepared ceria surface exhibiting the low temperature morphology are pyramidal islands discussed in detail in Section III.2.4. The compilation of NC-AFM images of Fig. 27 taken with different resolution on films annealed at various temperatures shows the high degree of regularity in pyramid formation and their thermal stability. The only feature that significantly changes as a function of annealing temperature in the range from 510 K to 790 K is the formation of spikes rising to a height above the highest pyramids. These very sharp spikes grow mostly between the pyramids and have a width of less than 3 nm; the density and height of the spikes increases with annealing temperature, however, the spikes can be removed by annealing the film to 850 K, a temperature leaving the pyramids entirely unchanged. The origin of the spikes could not be clarified so far, however, we speculate that they result from contaminants in the film or in the praseodymia buffer layer segregating to the film surface.

The transformation of the ceria film into the high temperature morphology occurs for annealing at temperatures in the

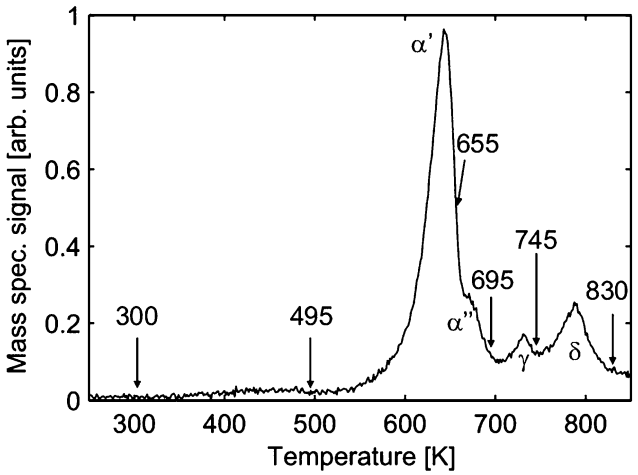

Fig. 22 Temperature programmed desorption spectrum (heating rate 1 K s^{-1}) of molecular oxygen for a 16 nm thick PrO_2(111) film. After a certain characteristic desorption peak is observed the desorption is stopped (arrows) and the sample is immediately cooled to RT to perform GIXRD experiments. (Reproduced from ref. 107.)

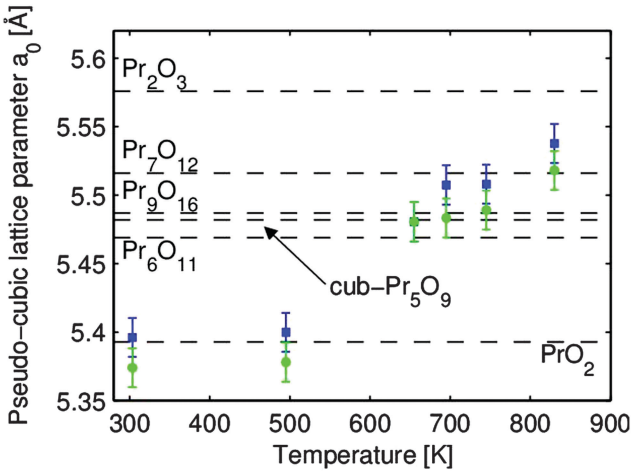

Fig. 24 The pseudo-cubic lattice constants a_0 of the two coexisting praseodymia phases related to thermal reduction. The lattice constants are determined under consideration of the elastic deformation of the film. The bulk values of the praseodymia phases stable at room temperature are marked by dashed lines. (Reproduced from ref. 107.)

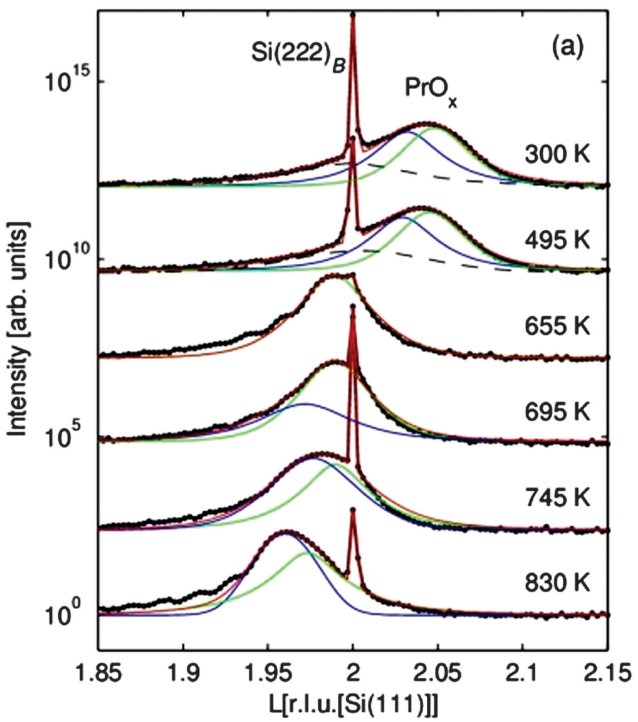

Fig. 23 XRD measurements of the region close to the $(222)_B$ Si Bragg peak for samples quenched at different temperatures. The oxide peak is described by two Lorentzian functions representing two laterally coexisting praseodymia phases. For the non-reduced films, an additional broad peak (dashed lines) is observed which can be attributed to a very thin Pr_6O_{11}(111) interface layer. (Reproduced from ref. 107.)

range of 930 K to 1100 K. The respective surface structure and that of preceding transition states are shown in Fig. 28(a) to (j). The onset of the transformation observed for annealing the sample at 930 K is shown in Fig. 28(a) to (c). The pyramidal structure is gradually dissolved into rounded, flat islands as relicts marking the position of former pyramidal islands (see triangles in Fig. 28(b)). The flat islands have a much larger contiguous surface area with (111) orientation and exhibit terraces with a width of 10 nm to 15 nm. While most terraces are separated by one triple-layer high step edges, the height of some step edges amounts to several triple-layers indicating that step-bunching occurs during the transformation of the islands.

When annealing the film at 1060 K, the average extension of the terraces increases significantly and the transformation into the high temperature morphology is completed as shown in Fig. 28(d) to (j). Terraces formed during such preparations have a width of 50 nm to 60 nm that is significantly larger than the width of terraces on similarly prepared bulk single crystal surfaces. The final results are hexagonal pits and protrusions with mostly straight step edges so that the nanoscale morphology is very similar to the one found for the surface preparation of bulk single crystals.[23,26,29] In contrast to similarly prepared surfaces of bulk ceria crystals developing perfect atomic regularity on terraces, surfaces of the film exhibit many atomic scale irregularities that are clearly seen in high resolution images compiled in Fig. 28(i) to (k). These irregularities yield a specifically strong local KPFM contrast as demonstrated in Fig. 28(f) indicating the presence of local charge or polarisation in or underneath the surface. The irregularities prevail even after the sample has been prepared with Ar^+ ion sputter cycles and annealing at 1090 K. As the transformation into the high temperature morphology is accompanied by a strong reduction of the ceria film (see Section III.2.5.2), we speculate that the irregularities are the result of oxygen vacancy clusters appearing during reduction.

When annealing the ceria film at temperatures higher than 1100 K, the surface undergoes a major change. As seen in Fig. 28(k), large hexagonally shaped hillocks having a lateral extension of several hundreds of nanometres separated by 100 nm deep trenches are formed. This dramatic change in morphology is the result of a decomposition of the film related to the formation

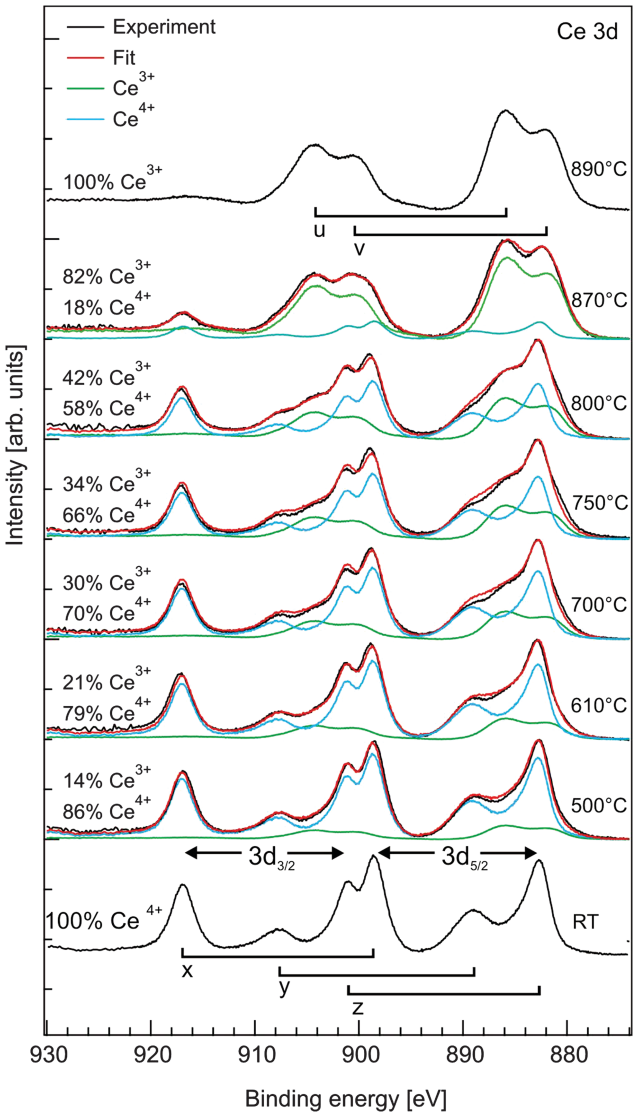

Fig. 25 Ce 3d region measured by XPS for a 250 nm CeO_2(111) film. The areas under the peaks are normalised to unity after a Shirley background is subtracted. The reference spectrum of CeO_2 is measured after plasma cleaning of the samples and consists of three peaks (*x*, *y*, *z*) in each $3d_{5/2}$ and $3d_{3/2}$ component. The surface near the region is fully reduced to Ce_2O_3 with two peaks (*u*, *v*) in each $3d_{5/2}$ and $3d_{3/2}$ component after annealing at 890 °C. The Ce^{3+}/Ce^{4+} ratio of the intermediate states is determined by fitting with a weighted linear combination of the CeO_2 and Ce_2O_3 spectra. (Reproduced from ref. 97.)

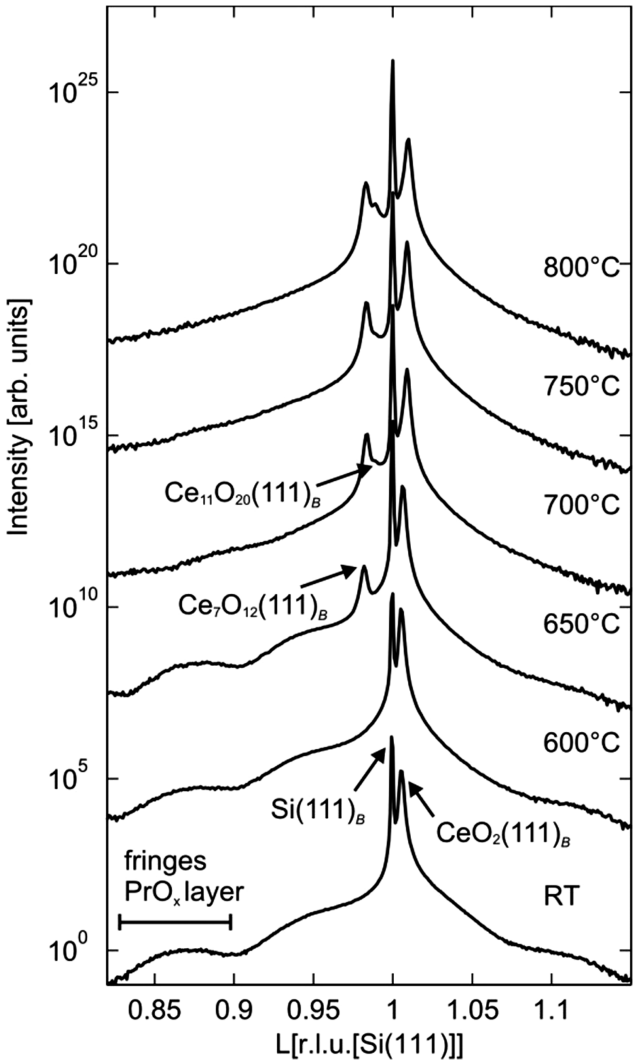

Fig. 26 Specular (00*l*) XRD scans close to the $Si(111)_B$ Bragg peak after annealing at temperatures up to 800 °C for 30 min. After annealing at 650 °C Ce_7O_{12}(111) Bragg peaks appear at lower *l* values than the CeO_2(111) peak. A third peak attributed to $Ce_{11}O_{20}$(111) becomes visible at temperatures after annealing at 700 °C. (Reproduced from ref. 97.)

of silicate and silicide at the interface to the Si(111) substrate as outlined in the XPS and XRD parts of Section III.2.5.2.[97] As for praseodymia, the different states of the films are reflected by their optical properties as illustrated by the photos shown in Fig. 28(l). The low temperature and high temperature states are characterised by shiny purple/blue and green/blue colours, respectively, while the decomposed film attains a dull grey colour.

In summary, the as-grown ceria films exhibit metastable surface structures in the form of terraced pyramids grown in the ⟨111⟩ direction with the base oriented in ⟨−1−12⟩ directions. In this low temperature morphology, the surface exhibits an exceptionally large number of edges and kink sites at step edges exclusively having a height of one O–Ce–O triple-layer. When the film is annealed to temperatures between 930 K and 1100 K, the pyramids undergo a phase transition into large terraces separated by steps with predominantly one O–Ce–O triple-layer height but also some higher steps. The properties of the film surface with this high temperature morphology resemble those of ceria crystals; however, the film exhibits exceptionally large terraces. Having distinctly different morphological characteristics, the film is in both states very well defined and ordered at the nanoscale. Provided it will be possible to remove the atomic scale irregularities by further efforts in a refined post-deposition treatment, for instance, involving a controlled re-oxidation of thermally treated films, the ceria film is a perfect model system for ceria surface studies but can also be used for applications requiring either a large number of edge and kink sites or large atomically flat terraces.

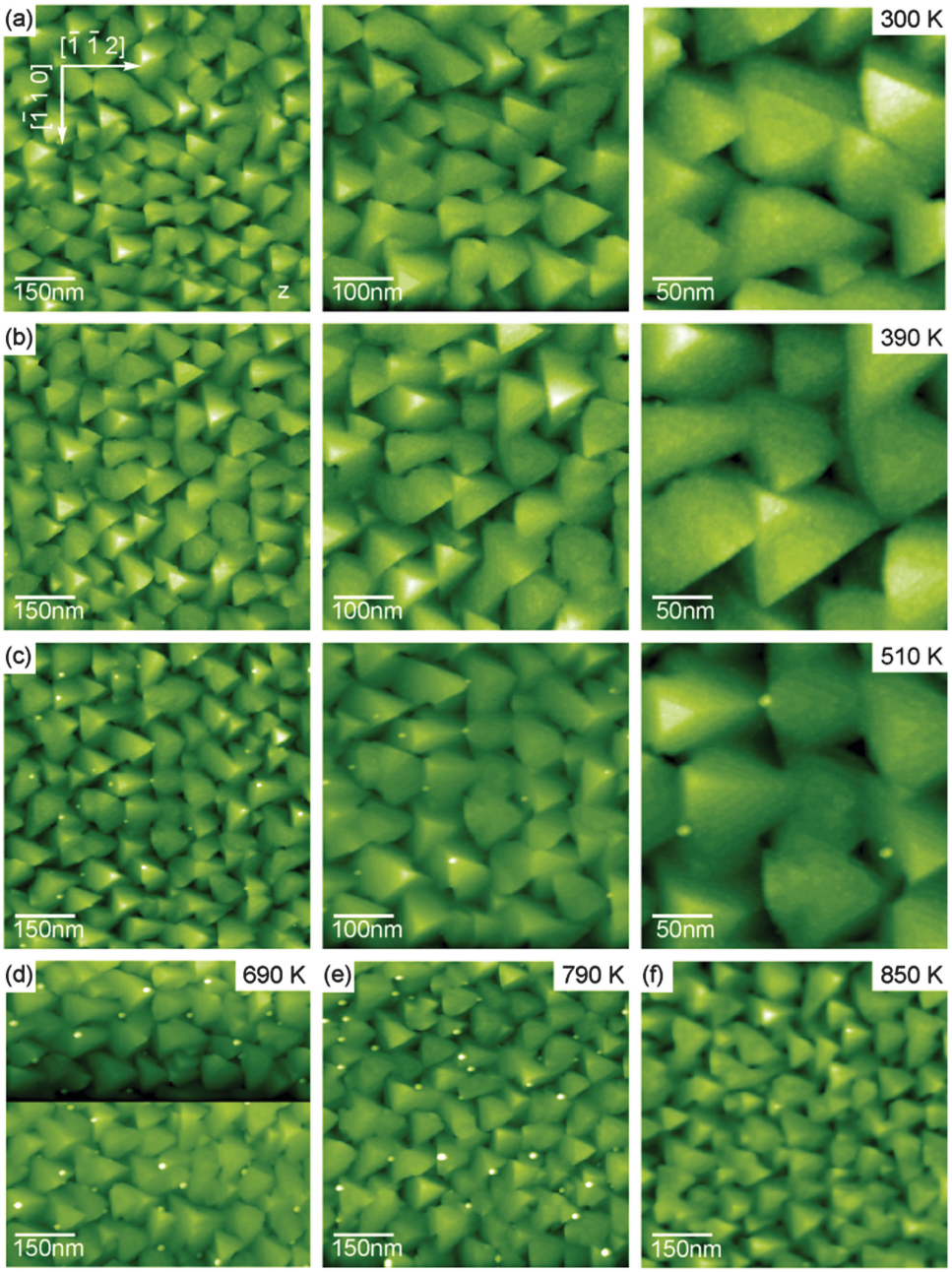

Fig. 27 Selected NC-AFM images of 180 nm thick cub-CeO_2(111) films representing the low temperature morphology. Films have been annealed to temperatures of (a) 300 K (as prepared sample), (b) 390 K, (c) 510 K and (d) to (f) 690 K, 790 K and 850 K, respectively. Images in rows (a)–(c) were taken under identical conditions with only the frame size varied. Dot-like bright features appearing in frames (c) to (e) are commented in the main text. (Reproduced from ref. 131.)

III.2.6 Reducing $Ce_{1-x}Pr_xO_{2-\delta}$. It has frequently been reported that doping of CeO_2 with trivalent cations induces additional $V_O^{\bullet\bullet}$, lattice distortion and, thus, enhances the oxygen storage/release capacity and the ionic conductivity of ceria.[110,139–142] Therefore, we investigate the reduction behaviour of the ternary single crystalline film $Ce_{1-x}Pr_xO_{2-\delta}$ as a function of the doping level $x = 0.2$, 0.4 and 0.6 by means of TPD, XRD, XPS and Raman spectroscopy.[143]

The oxygen release from *in situ* plasma-oxidised samples (“clean surfaces”) is investigated by TPD where the results (shown in Fig. 29(a)) reveal that as the Pr concentration x is increased, the samples release O_2 at lower temperatures compared to bulk CeO_2 films, what is attributed to the high oxygen exchange activity of the Pr^{4+}/Pr^{3+} system. From the results shown in the inset of Fig. 29(a), we conclude that the oxygen storage effect is mainly based on the Pr^{4+}/Pr^{3+} redox system as the ratio between the integrated O_2 TPD signal and the film thickness I_{O_2}/t increases linearly with x. In contrast, *ex situ* atmosphere exposed samples (“hydrocarbon covered surfaces”) show inverse results, namely, the release of oxygen in the form

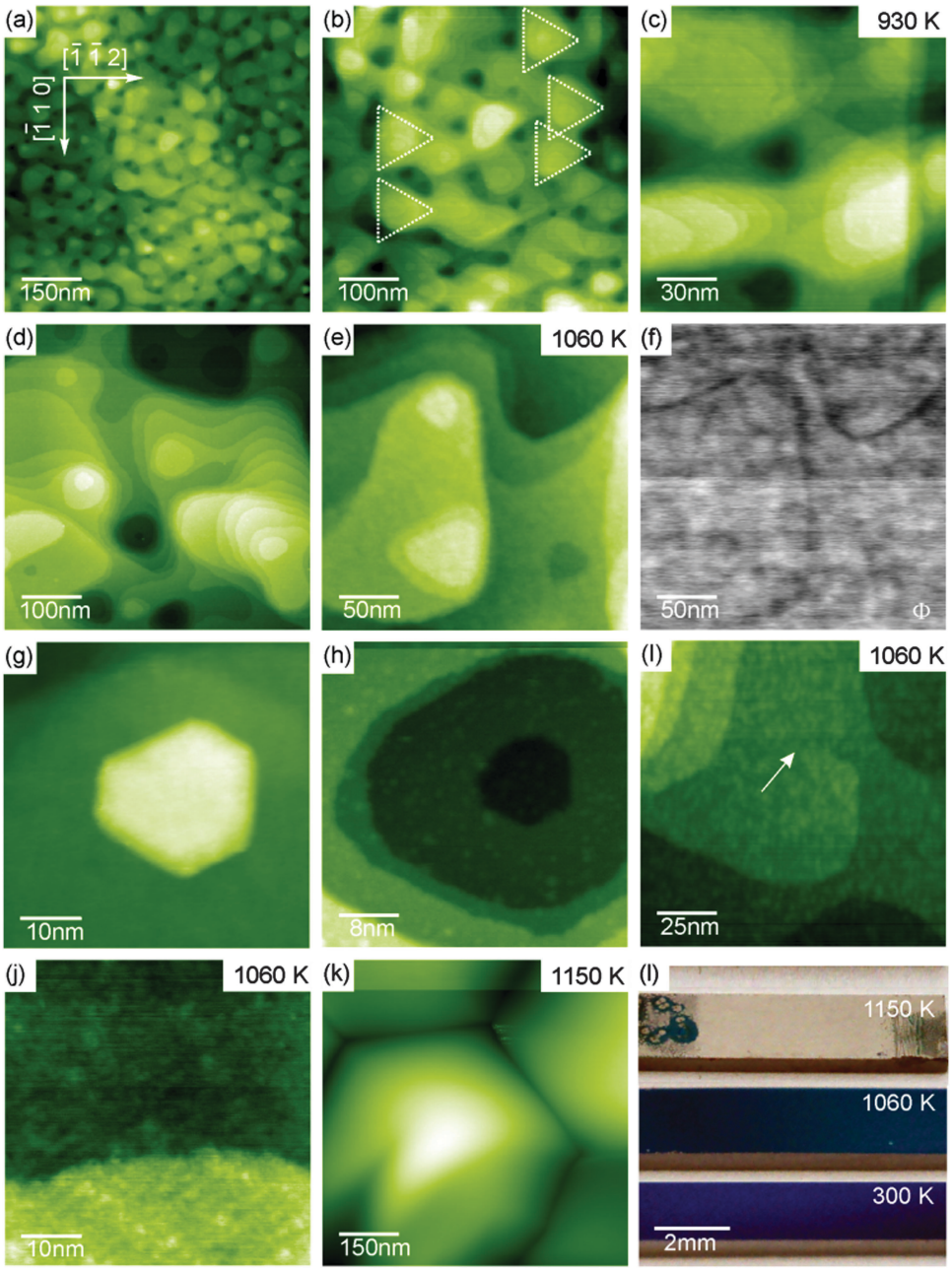

Fig. 28 Selected NC-AFM and KPFM images of 180 nm thick cub-CeO_2(111) films representative for the high temperature morphology and the decomposed film. Films were annealed to temperatures of 930 K (a) to (c), 1060 K (d) to (j) and 1150 K (k). The photos in (l) illustrate the change in optical properties of the films yielded by treatment at different temperatures. (Reproduced from ref. 131.)

of H_2O, CO and CO_2, where the desorption peak is shifted towards lower temperatures with decreasing x (*i.e.* more Ce in the mixed oxide) as demonstrated in Fig. 29(b). The fact that oxygen is not released as O_2 could be attributed to a kinetically favoured reaction path of hydrocarbon oxidation instead of oxygen recombination. Moreover, ceria has a superior hydrocarbon oxidation capability, better than praseodymia, lowering the CO_2 desorption temperature in Ce richer samples.[144] However, no significant Ce^{4+}/Ce^{3+} valence state change is found during the annealing in the temperature range from 200 °C to 300 °C as revealed by an XPS analysis.[143] It is possible that an oxygen transport occurs to Ce^{3+} by the reduction of Pr^{4+}, since the oxygen prefers to locate around Ce ions[145] and, therefore, praseodymia serves as an oxygen reservoir in the mixed oxide.

Complementary to the oxygen release, the reduction state of the sample with a hydrocarbon covered surface is revealed in an indirect way by measuring the temperature dependent lattice spacing variation Δd_{222} extracted from XRD measurements yielding the results shown in Fig. 29(c). The lattice spacing clearly increases with increasing temperature and this can be attributed to the Pr^{4+}/Pr^{3+} transition because the ionic radius of Pr^{3+} is larger than that of Pr^{4+}. The lattice spacing variation

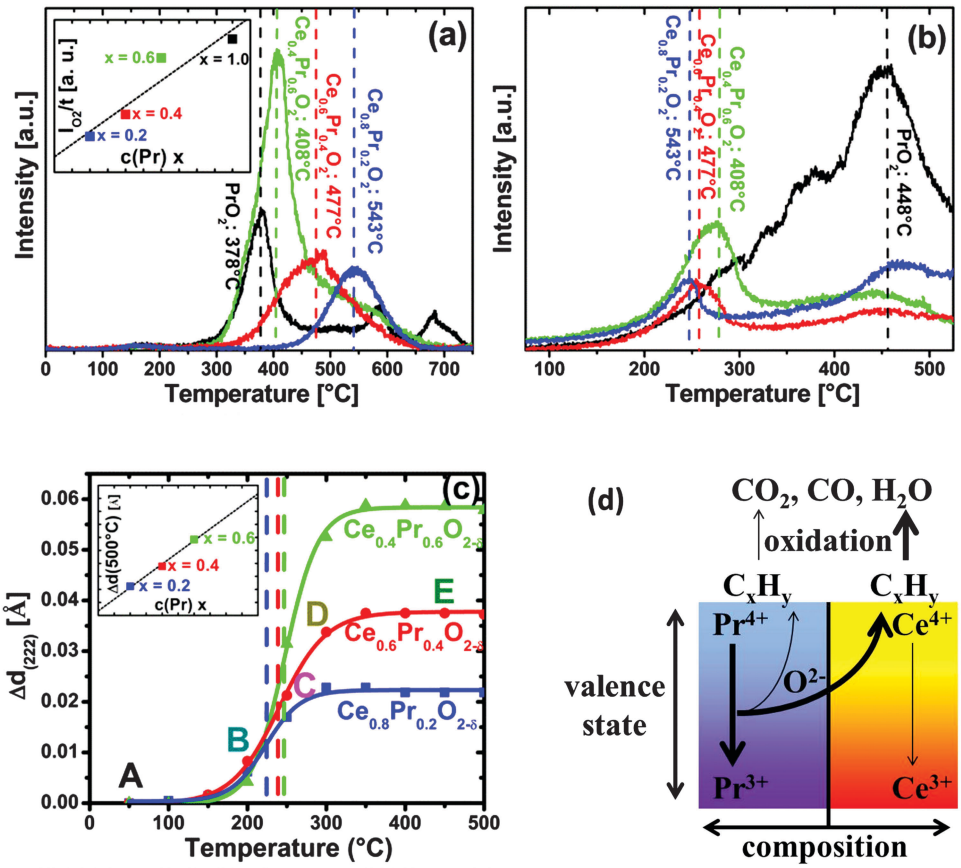

Fig. 29 (a) TPD spectra of O_2 for $Ce_{1-x}Pr_xO_{2-\delta}$(111)/Si(111) samples treated *in situ* with oxygen plasma with the inset showing the I_{O_2}/t *versus* x plot. (b) TPD spectra of CO_2 for the same samples treated *ex situ* with molecular oxygen. (c) Temperature dependent Δd_{222} of the same samples exposed to the ambient atmosphere with the inset showing Δd_{222}(500 °C) as a function of x. (d) Model of the $Ce_{1-x}Pr_xO_{2-\delta}$ redox process. (Reproduced from ref. 143.)

Δd_{222} (500 °C) increases linearly with x as shown in the inset of Fig. 29(c). This indicates that also for the mixed oxide with a hydrocarbon covered surface, the oxygen release is mainly triggered by the Pr^{4+}/Pr^{3+} redox system.

Based on these results, a reduction model for $Ce_{1-x}Pr_xO_{2-\delta}$ has been developed that is schematically shown in Fig. 29(d). While the OSC is supported by the Pr^{4+}/Pr^{3+} redox system (thick arrow in the purple region), the hydrocarbon oxidation capability originates from the Ce^{4+}/Ce^{3+} redox system (thick arrow crossing the purple and yellow region). Since Ce favours the +4 valence state more than Pr, in the mixed oxide an exchange occurs by oxygen transport to Ce^{3+} (and mainly to the surface region) accompanied by the reduction of Pr^{4+}. The oxygen mobility is provided by oxygen vacancies playing an important role for such kinds of oxidative processes.[145]

IV. Adsorption of methanol on CeO_x, PrO_x and $Ce_{1-x}Pr_xO_{2-\delta}$ films

Methanol oxidation has been well established as a test reaction for characterising the surface of metal oxide catalysts, allowing for a quantification and classification of active sites.[146,147] Their chemical properties, rendering the oxide, for instance, an acid–base or a redox catalyst, can be deduced from the spectrum of surface species and products evolving after the exposure to methanol. Chemisorption of methanol on oxides is often observed to break the OH bond, generating methoxy species $(CH_3O)_{ads}$ at the surface.[148–151] While acidic sites lead to the formation of coupling products and at basic sites typically complete dehydrogenation of the surface methoxy is observed as indicated by CO or CO_2 desorption, dehydrogenation is more selective on redox catalysts and, hence, formaldehyde (CH_2O) desorbs as a major product at elevated temperatures.[146,147]

Among the range of REOs, ceria has, so far, been the primary target of surface science studies on oxide-catalysed methanol oxidation. Besides ceria crystal surfaces[152] also epitaxial cerium oxide thin films of various thicknesses on different substrates such as α-Al_2O_3, Y-stabilised zirconia, Nb-doped $SrTiO_3$(100), Cu(111), and Ru(0001) have been studied as model systems for ceria catalysts.[50,57,152–154] In the following, common findings of these studies as well as differences are pointed out.

Consistently, physisorption of methanol multilayers was found at temperatures below 140 K. Desorption of these multilayers and of a chemisorbed methanol monolayer is observed between 140 K and 200 K,[50,154] leaving predominantly methoxy and OH groups on the surface.[50,152,153] Their formation from methanol goes along with the reduction of Ce and, obviously,

consumes oxygen from the ceria lattice.[50] More dissociative methanol adsorption was found on reduced ceria films than on fully oxidised films.[57,152,154] The species H_2O, CH_2O, H_2, CO, and CO_2 were the only products of methanol oxidation detected during TPD at elevated temperatures ($T > 200$ K).[57,153,154] While on CeO_2(111) predominantly H_2O and CH_2O are observed, indicating selective dehydrogenation of the methoxy, also CO and H_2, *i.e.* products of complete dehydrogenation were found to desorb from partially reduced ceria surfaces.

Besides common trends, previous studies also found distinct differences between measurements revealing dependencies of methanol oxidation not only on the Ce valency but also on details of the cerium oxide film preparation and on the surface structure. Comparing 19 nm thick CeO_2(100) films grown on Nb-doped $SrTiO_3$(100) and 5 nm thick CeO_2(111) films grown on Ru(0001), Mullins and co-workers found that the CeO_2(100) surface, which presumably exhibits more under-coordinated Ce and O sites than CeO_2(111), has a higher activity for methanol oxidation and shows a trend towards more extensive decomposition of methanol.[57] Besides methoxy, which was the only prevalent carbonaceous species found by Mullins and co-workers in their studies,[57,154] Matolín and co-workers also detected formate $(CHOO^-)_{ads}$ as a resident on the surface of 1.5 nm thick CeO_2(111) films grown on Cu(111),[50] indicating, besides complete dehydrogenation, a second route of methanol oxidation on these films directly involving lattice oxygen.

In the present work, the reported dependencies of activity and selectivity of reactions on REO surface composition are tested by exposing epitaxial cerium oxide, praseodymium oxide, and mixed $Ce_{0.4}Pr_{0.6}O_{2-\delta}$ films grown as detailed in Section III.1 to methanol. In contrast to previous work, where reduced cerium oxide surfaces were prepared by repeatedly exposing ceria films to methanol, which provides only limited control of the oxidation state, three well characterised cerium oxide film surface stoichiometries, namely CeO_2, Ce_7O_{12} and Ce_2O_3 are prepared by plasma and thermal treatments as described in Section III.2.5.2. Also for praseodymia, methanol oxidation is studied on the fully oxidised phase (PrO_2), a partially reduced film with a stoichiometry close to Pr_6O_{11}, and a film fully reduced at the surface as described in Section III.2.5.1. The role of the rare earth valency for the selectivity of methanol dehydrogenation at the model REO catalysts is the focus of combined TPD and XPS experiments.

For TPD, a UHV chamber with a base pressure of 10^{-8} Pa is available that is equipped with a quadrupole mass spectrometer, LEED and an UHV-compatible RF plasma source for oxygen plasma treatment as described in Section II.2. SR-XPS experiments are performed in a separate UHV chamber at MAX IV laboratory at Beamline D1011 in Lund, Sweden. At both sites, samples from the same Si wafers, on which 15 nm thick ceria, 16 nm thick praseodymia and 23 nm thick mixed $Ce_{0.4}Pr_{0.6}O_{2-\delta}$ films have been grown are used for parallel investigation. The REO films are initially fully oxidised by oxygen plasma treatment and then thermally reduced while the surface structure is monitored by LEED to observe, for instance, the characteristic pattern of the Ce_7O_{11} phase.[138]

Prior to TPD measurements, the samples are exposed to 15 L methanol at a sample temperature of 105 K by a gas doser directed to the sample surface. The sample is then placed close to the aperture of a quartz cap surrounding the mass spectrometer so that only products desorbing from the sample surface are collected. During TPD, a heating rate of 1 K s^{-1} is maintained by an electronic controller. To detect the carbonaceous products CO, CH_2O, and CO_2, atomic masses 28, 29, and 44 are monitored as CHO is the most abundant fragment of CH_2O after electron ionisation in the mass spectrometer. The number of recorded masses is restricted to maintain sufficiently fast data recording.

For SR-XPS experiments, samples are exposed to 15 L methanol at a sample temperature of 100 K to 120 K by backfilling the UHV chamber. The samples are then heated in intervals up to a maximum temperature that is step-wise increased in analogy to procedures described in ref. 50. After each heating interval with the maximum temperature maintained for 1 min, the sample is cooled down to ~140 K and SR-XPS data are recorded. In this way, a series of XP spectra are obtained with each spectrum being representative of the resident surface species present at the respective maximum temperature.

IV.1 Methanol oxidation on CeO_x

TPD experiments on ceria shown in Fig. 30 are referenced to previous work[50,57,154] identifying the temperature range above 200 K as relevant in terms of detecting carbonaceous products of methanol oxidation. In accordance with this previous work, the spectral intensities of masses 28 and 29 observed at temperatures below 200 K for CeO_2 and Ce_7O_{12} can be interpreted as fragments of methanol[155] desorbing from physisorbed multilayers or from a chemisorbed methanol layer leaving methoxy species at the surface. At elevated temperatures, no desorption of formaldehyde is detected from CeO_2(111) films, however, significant amounts of CO and CO_2 are produced, visible as broad desorption peaks centred at ~600 K in Fig. 30 indicating complete oxidation of methanol at the surface. Formaldehyde desorption at ~600 K as an indicator for selective dehydrogenation is only observed from the partially reduced surface Ce_7O_{12} concomitantly with CO and CO_2 desorption. While the CO signal comprises ionisation-induced fragments from CH_2O and CO_2, these contributions account for less than 50% of its intensity as a quantitative analysis of the desorption peak intensities at masses 28, 29, and 44 reveals. This implies that CO is also produced at the Ce_7O_{12} surface.

After exposing the Ce_2O_3 surface to methanol at 105 K, TPD yields no evolution of products at all. Even below 200 K, no fragments of methanol desorption are detected. This puzzling result observed in repeated experiments indicates that methanol adsorption on the fully reduced cerium oxide film is negligible and, therefore, also its activity for methanol oxidation is negligible.

Methanol oxidation on ceria films does not match previously observed trends.[57,152,154] Quite opposite, complete oxidation and significant activity is observed on fully oxidised CeO_2(111) while the partially reduced surface with Ce_7O_{12} stoichiometry tends to catalyse selective dehydrogenation of methanol.

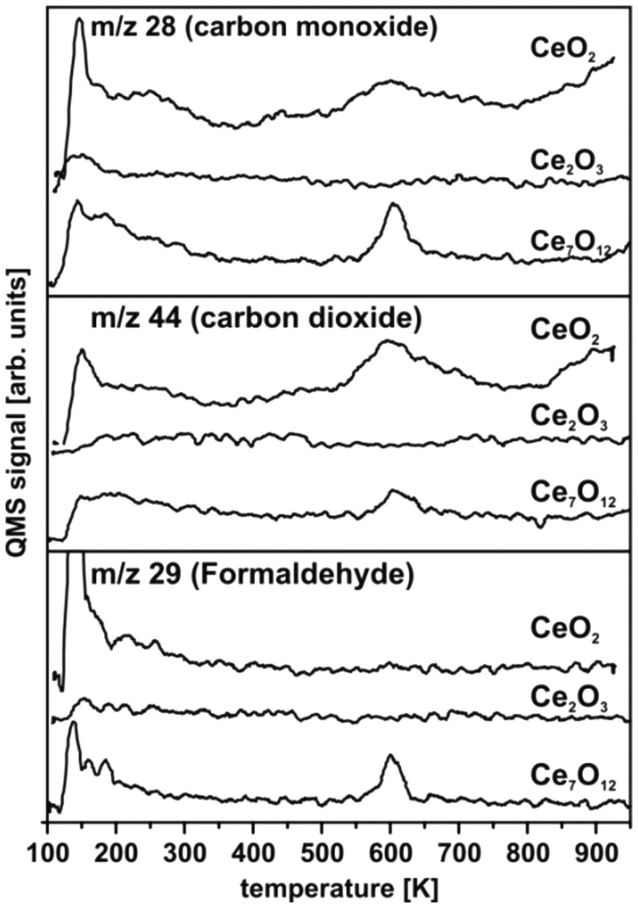

Fig. 30 TPD spectra of methanol adsorbed on ceria surfaces of different oxidation states. Only the partially reduced Ce_7O_{12} surface yields CH_2O. On CeO_2 total oxidation is observed while the Ce_2O_3 surface shows no reactivity towards methanol.

Furthermore, the present study does not indicate an increased amount of methanol adsorbed on reduced ceria as compared to CeO_2. In fact, the fully reduced Ce_2O_3 surface exhibits the lowest sticking coefficient for methanol. Details of the surface morphology and defect structure, both depending, for instance, on substrate, growth conditions, and film thickness very likely play a prominent role for the different trends observed here and in previous studies.

IV.2 Methanol oxidation on PrO_x

SR-XPS data for the C 1s binding energy region provide insight into carbonaceous species resident on the surface after methanol adsorption on PrO_2 and Pr_2O_3 and subsequent heating with respective results shown in Fig. 31(a) and (b). The fully stoichiometric $PrO_2(111)$ surface exhibits a minor residual surface contamination by carbon (the "as-prepared" curve in Fig. 31(a)) and OH groups (the O 1s spectrum not shown), detected due to the high sensitivity of the SR-XPS experiment. No contamination is found on the fully reduced Pr_2O_3 surface. After methanol exposure at 100 K to 120 K, an intense C 1s peak at 287.7 eV observed for both, PrO_2 and Pr_2O_3 (grey curves in Fig. 31), provides evidence for methanol at the surface, probably with multilayer coverage. The shift of this peak to $\sim$287.0 eV and the decrease of its intensity upon heating PrO_2 and Pr_2O_3 up to 290 K and 300 K, respectively, indicate the desorption of methanol and the formation of methoxy species on the surface as previously reported for ceria.[50,154] Besides methoxy, also formate species are formed on the surface between 200 K and 400 K as revealed by C 1s peaks at binding energies between 289 eV and 290 eV detected for both PrO_2 and Pr_2O_3. The variation of the C 1s binding energy (289.0 eV on PrO_2 and 289.7 eV on Pr_2O_3 at 400 K) corresponds to that observed for formate adsorption on fully

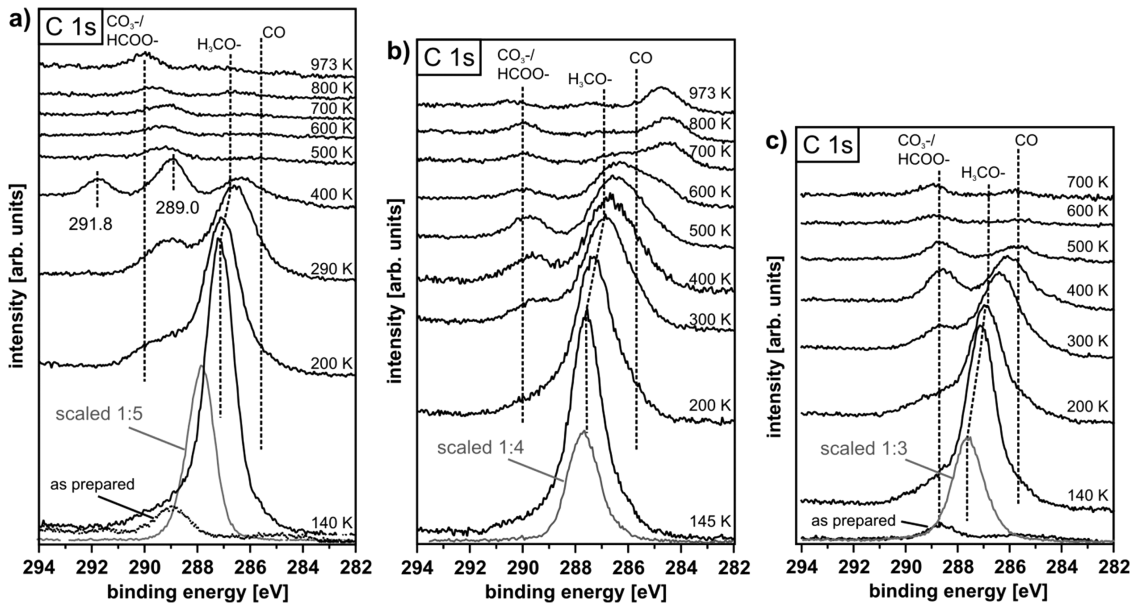

Fig. 31 C 1s core level spectra recorded at 410 eV photon energy after methanol adsorption and subsequent heating to the temperatures indicated for 16 nm thick PrO_2 (a) and Pr_2O_3 (b) films as well as a 23 nm thick $Ce^{4+}_{0.4}Pr^{3+}_{0.6}O_{1.7}$ (c) film after thermal reduction. Shown in addition: spectra of the REO film before methanol exposure denoted "as-prepared" and spectra recorded directly after methanol exposure before the initial heating interval shown as grey curves.

oxidised and partially reduced ceria.[156] The build-up of formate on the surface shows that, besides complete dehydrogenation, there is another route for methanol oxidation, as it has previously been reported for the CeO_2/Cu(111) system.[50] For PrO_2, SR-XPS even reveals a third carbon species with a C 1s binding energy of 291.8 eV on the surface at 400 K, indicating carbonate (CO_3^{2-}) formation on the cost of even more oxygen taken from the praseodymia lattice. Upon heating PrO_2 above 400 K and Pr_2O_3 above 600 K, the C 1s peak intensities strongly decrease, implying that carbonaceous products desorb above these temperatures.

The results from TPD after exposing PrO_2 and films with stoichiometries close to Pr_6O_{11} and to Pr_2O_3 to methanol at 105 K are shown in Fig. 32. Below 200 K, the detection of masses 28 and 29 indicates desorption of physisorbed and chemisorbed methanol in agreement with TPD and SR-XPS data for ceria. A strong CO_2 desorption peak and concomitantly CO desorption are observed from PrO_2 films at 480 K. Formaldehyde desorption is only minor, showing that complete oxidation of the methanol, obviously by consumption of lattice oxygen, is favoured. The grey curve in the top panel of Fig. 32 represents TPD of oxygen from an as-prepared PrO_2(111) film, *i.e.* without surface methoxy species. From as-prepared PrO_2, the desorption of lattice oxygen starts at ~500 K, hence, surface methoxy promotes the release of lattice oxygen from PrO_2, possibly *via* intermediate oxidation products such as surface formate and carbonate. From 500 K up to higher temperatures, the maxima of CO desorption from PrO_2 correlate with the maxima of oxygen release from the as-prepared PrO_2 film (grey curve), *i.e.* they coincide with REO reduction during phase transitions.

For a partially reduced film close to the Pr_6O_{11} stoichiometry prepared by heating PrO_2(111) up to 655 K, the detection of masses 28, 29, and 44 in TPD up to 400 K is ascribed to methanol desorption as discussed before and in accordance with XPS results (not shown), we observe a shift of the C1 s binding energy from 287.7 eV to 287.2 eV. No further product desorption is detected up to temperatures of 655 K. The increasing CO and CO_2 desorption above this temperature indicates a complete oxidation of surface resident carbonaceous species by the lattice oxygen that is expected to be released when Pr_6O_{11} is thermally reduced.

For the fully reduced Pr_2O_3 surface produced by heating a PrO_2 film up to 830 K (SR-XPS results not shown exhibit Pr only in the oxidation state 3^+), it should be noted that, opposite to the surface, the entire film may not be fully reduced.[107] Up to 655 K, TPD results obtained after methanol exposure at 105 K are qualitatively similar to those of the partially reduced praseodymia surface. At 680 K, a weak formaldehyde desorption peak is observed and concomitantly CO and CO_2 are produced. Increasing CO and CO_2 desorption as the temperature is raised above 830 K is ascribed to a decomposition of the praseodymia film accompanied by further release of lattice oxygen.

As for ceria, it is the fully oxidised PrO_2 film exhibiting a trend towards full oxidation of methanol while desorption of formaldehyde is observed only from the fully reduced surface, indicating selective dehydrogenation of adsorbed methoxy catalysed by Pr_2O_3. PrO_2 and the partially reduced Pr_6O_{11} film are not stable up to the desorption temperature of CH_2O from Pr_2O_3,

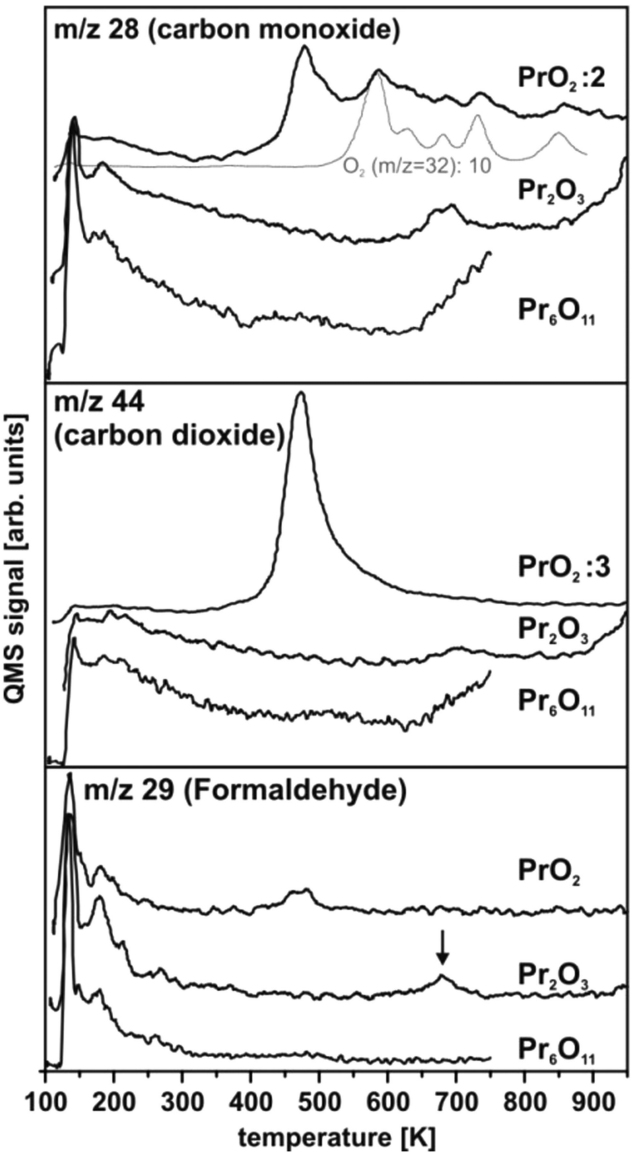

Fig. 32 TPD spectra of methanol adsorbed on surfaces of 16 nm thick praseodymia films in different oxidation states. A large CO_2 and CO desorption signal is observed for PrO_2 ~20 K below the onset of lattice oxygen desorption from an as-prepared PrO_2 film (grey spectrum, top panel). Pr_2O_3 only shows weak CO/CO_2 signals as well as a weak CH_2O signal (arrow, bottom panel). Pr_6O_{11} is rather unreactive towards methanol adsorption up to 655 K.

and the release of lattice oxygen below 680 K fully oxidises surface methoxy before formaldehyde can be formed. Of all ceria, praseodymia, and mixed oxide films studied, PrO_2 shows the highest activity for methanol oxidation below 500 K.

IV.3 Methanol oxidation on mixed $CePrO_x$

Partially reduced $Ce_{0.4}Pr_{0.6}O_{2-\delta}$ films are prepared from the fully oxidised state (δ = 0) when heating up to ~900 K. The LEED pattern recorded during heating indicates the presence of the ι-phase.[138] SR-XPS of the reduced films shows Ce exclusively in the oxidation state 4+ and for Pr exclusively 3+ valency (data not shown), yielding the stoichiometry $Ce_{0.4}Pr_{0.6}O_{1.7}$.

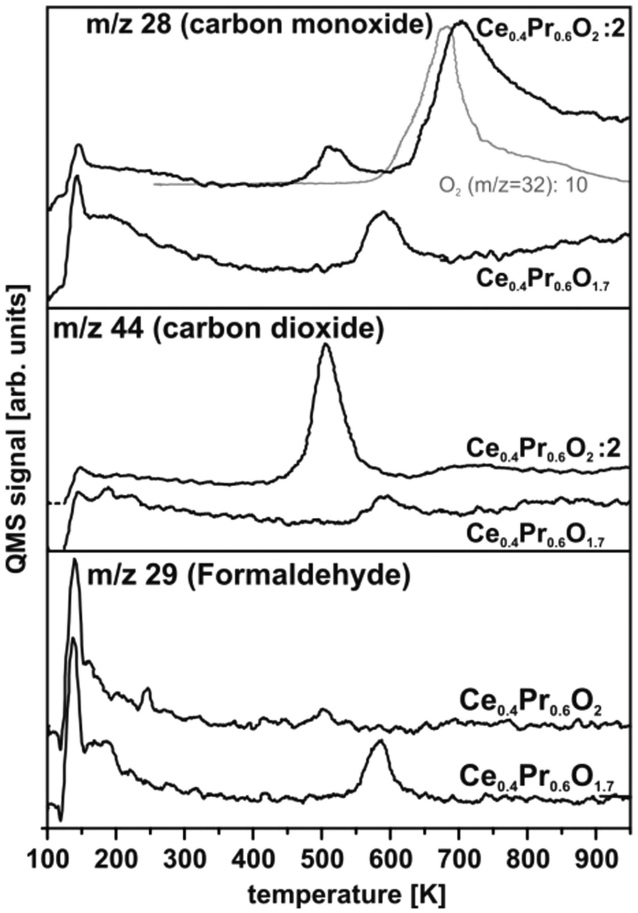

Fig. 33 TPD spectra of methanol adsorbed on surfaces of 23 nm thick $Ce_{0.4}Pr_{0.6}O_{2-\delta}$ films in different oxidation states. The partially reduced oxide shows selectivity towards CH_2O formation.

TPD results shown in Fig. 33 obtained after exposing the $Ce_{0.4}Pr_{0.6}O_2$ film to methanol are qualitatively similar to those obtained for PrO_2. At 500 K, a pronounced CO_2 desorption peak and concomitant CO desorption is observed, however, no formaldehyde, revealing full oxidation of adsorbed methanol. As for PrO_2, the CO_2 desorption peak is observed 20 K below the temperature at which the release of lattice oxygen starts from as-prepared $Ce_{0.4}Pr_{0.6}O_2$, *i.e.* without surface methoxy species (the grey spectrum in the top panel of Fig. 33 shows the desorption of O_2 from the as-prepared film). The CO_2 desorption temperature is 20 K higher for $Ce_{0.4}Pr_{0.6}O_2$ than for PrO_2 (peak at 480 K), indicating that Ce^{4+} present in the mixed oxide film impedes the reduction of Pr^{4+} and the release of lattice oxygen.

SR-XPS results of $Ce_{0.4}Pr_{0.6}O_{1.7}$ shown in Fig. 31(c) reveal the prevalence of surface methoxy after the desorption of physisorbed methanol multilayers and the build-up of formate species at temperatures up to ~500 K, as it is observed on the fully reduced praseodymia surface. TPD after exposing the $Ce_{0.4}Pr_{0.6}O_{1.7}$ film to methanol yields spectra shown in Fig. 33 that are similar to those observed for the Ce_7O_{12} phase. A formaldehyde desorption peak is observed at ~580 K and concomitantly also CO and CO_2 desorb as oxidation products.

In summary, praseodymia as well as ceria and mixed films exhibit a trend towards complete oxidation of methanol and, overall, a higher activity when they are fully oxidised. A selectivity towards partial dehydrogenation of surface methoxy formed by dissociative adsorption of methanol is observed for the partially reduced REO films. From the fully reduced Ce_2O_3 surface, no desorption of carbonaceous products is observed after exposure to CH_3OH at 105 K and also the Pr_2O_3 surface shows a comparatively low activity for methanol oxidation. The partially reduced films provide the best balance between activity and the often desired catalytic selectivity towards partial dehydrogenation and formaldehyde production. Mixed ceria/praseodymia films show a potential for creating a catalyst with a good balance between the high oxygen mobility in PrO_x and the high stability of CeO_x.

V. Conclusions

Rare earth oxides are well established as materials for a large variety of technical applications with chemical catalysis being the most prominent. The desired functionality for specific applications is often created by using complex systems with tailored macro-, micro- and nanostructures and a suitable composition of elements forming binary, ternary or even quaternary rare earth oxide systems. Among the many base materials used, praseodymia and ceria are outstanding with respect to their oxygen release, storage and transfer capability based on their exceptional stability properties with respect to phase transitions involving oxygen transfer. In a fully reversible process controlled by sample temperature and environment, oxygen can be removed in large amounts from the fully oxidised REO_2 state to form a variety of stable and atomically well-ordered intermediate oxide states until the fully reduced sesquioxide RE_2O_3 is reached while fully maintaining the structural integrity of the material throughout the series of phase transitions. While the oxygen transfer related phase diagrams for bulk samples of praseodymia and ceria have been explored in the past, in our work, we establish procedures for a controlled synthesis and post-deposition preparation of stable films to yield a system in any desired stoichiometry between the fully oxidised and fully reduced limiting phases. As a working platform well suitable for basic research model studies, we introduce the growth of rare earth oxides on Si(111) wafers by molecular beam epitaxy. High quality films can be grown as a binary oxide or a ternary oxide in the form of a mixed or layered material with a thickness ranging from a few to a few hundred nanometres. For ceria, we are able to very well define the surface morphology varied from a kinetically determined pyramidal nanostructure exhibiting a large number of steps and kinks at the atomic scale to a thermodynamically fully relaxed surface exhibiting large atomically flat terraces separated by a small number of single unit steps by a suitable post-deposition thermal treatment. Likewise, the stoichiometry of the surface can be tailored by thermal, gas exposure or plasma treatment, however, we find that for some intermediate states, a coexistence of phases is unavoidable. The film and surface structure can further be controlled by exploiting internal stress and relaxation

effects induced by the lattice mismatch at the substrate–film interface, which is specifically interesting for tailoring ternary systems. Our studies clearly reveal the capabilities and limitations of the oxide films in terms of oxygen transport capability as well as thermal and environmental stability. While praseodymia clearly sets the benchmark in oxygen mobility, ceria is superior regarding thermal and environmental stability. The opposite electrochemical properties of the Ce^{4+}/Ce^{3+} and Pr^{4+}/Pr^{3+} redox systems on the one hand and the crystallographic similarities allowing the formation of truly mixed systems on the other hand allows tailoring rare earth oxide systems with most interesting properties. Thus, in their great variety of possible compositions, structures, stoichiometries and surface morphologies, the films are equally suitable for thin film model system studies and industrial applications where robust, bulk-like samples are required. The preparation of films by standard techniques used in the semiconductor industry greatly facilitates the creation of nanostructured, specifically functionalised and integrated systems by lithography, implantation and contacting techniques. By mastering the enormous complexity of advanced rare earth oxide systems and providing a facile route for production, the established thin film synthesis platform creates a great potential for expanding our understanding of rare earth oxides used in chemical catalysis,[157–159] microelectronics, specifically resistive random-access memory devices,[160,161] energy technologies,[110,111,140,162] sensors[163,164] and many other fields of application such as magneto-optic or spintronic devices based on room temperature ferromagnetism.[118,120,165,166]

Acknowledgements

The authors gratefully acknowledge the funding of the project by the Deutsche Forschungsgemeinschaft *via* grants BA 1710/17-1, RE 1186/12-1, SCHR 1123/4-1, WO 533/16-1 and support from the COST Action CM1104. G. N. expresses his gratitude to the Alexander von Humboldt foundation for a post-doctoral fellowship. M.R. gratefully acknowledges stimulating discussions about film growth mechanisms with P. Maaß.

References

1 S. D. Barrett and S. S. Dhesi, *The Structure of Rare-Earth Metal Surfaces*, Imperial College Press, London, 2001.
2 K. C. Taylor, *Catalysis – Science and Technology*, Springer-Verlag, Berlin, 1984.
3 K. Otsuka, K. Jinno and A. Morikawa, *J. Catal.*, 1986, **100**, 353.
4 G. Adachi, N. Imanaka and Z. C. Kang, *Binary Rare Earth Oxides*, Springer, Dordrecht, 2004.
5 J. R. Jayaramaiah, B. N. Lakshminarasappa and B. M. Nagabhushana, *Sens. Actuators, B*, 2012, **173**, 234.
6 S. S. Kim, J. H. Moon, B.-T. Lee, K.-S. Sohn, T. S. Kang and J. H. Je, *Appl. Surf. Sci.*, 2004, **221**, 231.
7 S. Thakur, N. K. Sahoo, M. Senthilkumar and R. B. Tokas, *Opt. Mater.*, 2005, **27**, 1402.
8 D. P. Norton, *Mater. Sci. Eng., R*, 2004, **43**, 139.
9 www.itrs.net.
10 J. Stankiewicz, F. Villuendas and J. Bartolomé, *Phys. Rev. B: Condens. Matter Mater. Phys.*, 2007, **75**, 235308.
11 Y. A. Boikov, T. Claeson and D. Erts, *Phys. Rev. B: Condens. Matter Mater. Phys.*, 1997, **56**, 11312.
12 F. Sánchez, R. Bachelet, P. d. Coux, B. Warot-Fonrose, V. Skumryev, L. Tarnawska, P. Zaumseil, T. Schroeder and J. Fontcuberta, *Appl. Phys. Lett.*, 2011, **99**, 211910.
13 J. H. Choi, J. Y. Lee and Y. T. Kim, *Appl. Phys. Lett.*, 2000, **77**, 4028.
14 A. Fissel, R. Dargis, E. Bugiel, D. Schwendt, T. Wietler, J. Krügener, A. Laha and H. J. Osten, *Thin Solid Films*, 2010, **518**, 2546.
15 N. A. Bojarczuk, M. Copel, S. Guha, V. Narayanan, E. J. Preisler, F. M. Ross and H. Shang, *Appl. Phys. Lett.*, 2003, **83**, 5443.
16 G. Saint-Girons, P. Regreny, L. Largeau and G. Patriarche, *Appl. Phys. Lett.*, 2007, **91**, 241912.
17 F. A. Kröger and H. J. Vink, *Solid State Phys.*, Academic Press, 1956, vol. 3, p. 307.
18 Z. L. Wang and Z. C. Kang, *Functional and smart materials: structural evolution and structure analysis*, Plenum Press, New York, 1998.
19 G. Adachi and N. Imanaka, *Chem. Rev.*, 1998, **98**, 1479.
20 H.-W. Chiang, R. N. Blumenthal and R. A. Fournelle, *Solid State Ionics*, 1993, **66**, 85.
21 A. Trovarelli, *Catalysis by ceria and related materials*, Imperial College Press, London, 2002.
22 P. Fornasiero and A. Trovarelli, *Catalysis by Ceria and Related Materials*, Imperial College Press, London, 2014.
23 S. Torbrügge, M. Cranney and M. Reichling, *Appl. Phys. Lett.*, 2008, **93**, 073112.
24 S. M. F. Shahed, Y. Sainoo and T. Komeda, *Jpn. J. Appl. Phys.*, 2011, **50**, 08LB05.
25 N. Nilius, S. M. Kozlov, J. F. Jerratsch, M. Baron, X. Shao, F. Viñes, S. Shaikhutdinov, K. M. Neyman and H. J. Freund, *ACS Nano*, 2012, **6**, 1126.
26 H. H. Pieper, C. Derks, M. H. Zoellner, R. Olbrich, L. Tröger, T. Schroeder, M. Neumann and M. Reichling, *Phys. Chem. Chem. Phys.*, 2012, **14**, 15361.
27 H. H. Pieper, C. Lammers, L. Tröger, S. Bahr and M. Reichling, *Rev. Sci. Instrum.*, 2012, **83**, 055110.
28 S. Gritschneder, Y. Namai, Y. Iwasawa and M. Reichling, *Nanotechnology*, 2005, **16**, S41.
29 S. Gritschneder and M. Reichling, *Nanotechnology*, 2007, **18**, 044024.
30 P. S. Bagus, C. J. Nelin, E. S. Ilton, M. Baron, H. Abbott, E. Primorac, H. Kuhlenbeck, S. Shaikhutdinov and H. J. Freund, *Chem. Phys. Lett.*, 2010, **487**, 237.
31 D. C. Grinter, R. Ithnin, C. L. Pang and G. Thornton, *J. Phys. Chem. C*, 2010, **114**, 17036.
32 X. Shao, J. F. Jerratsch, N. Nilius and H. J. Freund, *Phys. Chem. Chem. Phys.*, 2011, **13**, 12646.
33 J. I. Flege, B. Kaemena, A. Meyer, J. Falta, S. D. Senanayake, J. T. Sadowski, R. D. Eithiraj and E. E. Krasovskii, *Phys. Rev. B: Condens. Matter Mater. Phys.*, 2013, **88**, 235428.

34 D. C. Grinter, C. L. Pang, C. A. Muryn, F. Maccherozzi, S. Dhesi and G. Thornton, *J. Electron. Spectrosc. Relat. Phenom.*, 2014, **195**, 13.
35 S. Torbrügge, M. Reichling, A. Ishiyama, S. Morita and O. Custance, *Phys. Rev. Lett.*, 2007, **99**, 056101.
36 M. V. Ganduglia-Pirovano, J. L. F. Da Silva and J. Sauer, *Phys. Rev. Lett.*, 2009, **102**, 026101.
37 Z. X. Yang, X. H. Yu, Z. S. Lu, S. F. Li and K. Hermansson, *Phys. Lett. A*, 2009, **373**, 2786.
38 C. J. Zhang, A. Michaelides, D. A. King and S. J. Jenkins, *Phys. Rev. B: Condens. Matter Mater. Phys.*, 2009, **79**, 075433.
39 J. F. Jerratsch, X. Shao, N. Nilius, H. J. Freund, C. Popa, M. V. Ganduglia-Pirovano, A. M. Burow and J. Sauer, *Phys. Rev. Lett.*, 2011, **106**, 246801.
40 G. E. Murgida and M. V. Ganduglia-Pirovano, *Phys. Rev. Lett.*, 2013, **110**, 246101.
41 Y. Pan, N. Nilius, H. J. Freund, J. Paier, C. Penschke and J. Sauer, *Phys. Rev. Lett.*, 2013, **111**, 206101.
42 V. Stetsovych, F. Pagliuca, F. Dvořák, T. Duchoň, M. Vorokhta, M. Aulická, J. Lachnitt, S. Schernich, I. Matolínová, K. Veltruská, T. Skála, D. Mazur, J. Mysliveček, J. Libuda and V. Matolín, *J. Phys. Chem. Lett.*, 2013, **4**, 866.
43 Y. G. Wang, D. H. Mei, J. Li and R. Rousseau, *J. Phys. Chem. C*, 2013, **117**, 23082.
44 T. Duchoň, F. Dvořák, M. Aulická, V. Stetsovych, M. Vorokhta, D. Mazur, K. Veltruská, T. Skála, J. Mysliveček, I. Matolínová and V. Matolín, *J. Phys. Chem. C*, 2014, **118**, 357.
45 S. M. Kozlov and K. M. Neyman, *Phys. Chem. Chem. Phys.*, 2014, **16**, 7823.
46 J. Kullgren, M. J. Wolf, C. W. M. Castleton, P. Mitev, W. J. Briels and K. Hermansson, *Phys. Rev. Lett.*, 2014, **112**, 156102.
47 S. Gritschneder, Y. Iwasawa and M. Reichling, *Nanotechnology*, 2007, **18**, 044025.
48 M. B. Watkins, A. S. Foster and A. L. Shluger, *J. Phys. Chem. C*, 2007, **111**, 15337.
49 M. Fronzi, S. Piccinin, B. Delley, E. Traversa and C. Stampfl, *Phys. Chem. Chem. Phys.*, 2009, **11**, 9188.
50 V. Matolín, J. Libra, M. Škoda, N. Tsud, K. C. Prince and T. Skála, *Surf. Sci.*, 2009, **603**, 1087.
51 C. Müller, K. Hermansson and B. Paulus, *Chem. Phys.*, 2009, **362**, 91.
52 C. Müller, B. Paulus and K. Hermansson, *Surf. Sci.*, 2009, **603**, 2619.
53 D. Fernández-Torre, K. Kośmider, J. Carrasco, M. V. Ganduglia-Pirovano and R. Pérez, *J. Phys. Chem. C*, 2012, **116**, 13584.
54 D. R. Mullins, P. M. Albrecht, T.-L. Chen, F. C. Calaza, M. D. Biegalski, H. M. Christen and S. H. Overbury, *J. Phys. Chem. C*, 2012, **116**, 19419.
55 S. Torbrügge, O. Custance, S. Morita and M. Reichling, *J. Phys.: Condens. Matter*, 2012, **24**, 084010.
56 D. R. Mullins and P. M. Albrecht, *J. Phys. Chem. C*, 2013, **117**, 14692.
57 P. M. Albrecht and D. R. Mullins, *Langmuir*, 2013, **29**, 4559.
58 N. Tsud, R. G. Acres, M. Iakhnenko, D. Mazur, K. C. Prince and V. Matolín, *J. Phys. Chem. B*, 2013, **117**, 9182.
59 D. Fernández-Torre, J. Carrasco, M. V. Ganduglia-Pirovano and R. Pérez, *J. Chem. Phys.*, 2014, **141**, 014703.
60 J.-L. Lu, H.-J. Gao, S. Shaikhutdinov and H.-J. Freund, *Catal. Lett.*, 2007, **114**, 8.
61 J. A. Rodriguez, X. Wang, P. Liu, W. Wen, J. C. Hanson, J. Hrbek, M. Pérez and J. Evans, *Top. Catal.*, 2007, **44**, 73.
62 M. Baron, O. Bondarchuk, D. Stacchiola, S. Shaikhutdinov and H. J. Freund, *J. Phys. Chem. C*, 2009, **113**, 6042.
63 N. J. Castellani, M. A. Branda, K. M. Neyman and F. Illas, *J. Phys. Chem. C*, 2009, **113**, 4948.
64 N. C. Hernández, R. Grau-Crespo, N. H. de Leeuw and J. F. Sanz, *Phys. Chem. Chem. Phys.*, 2009, **11**, 5246.
65 J. Majimel, M. Lamirand-Majimel, I. Moog, C. Feral-Martin and M. Tréguer-Delapierre, *J. Phys. Chem. C*, 2009, **113**, 9275.
66 M. Škoda, M. Cabala, I. Matolínová, K. C. Prince, T. Skála, F. Šutara, K. Veltruská and V. Matolín, *J. Chem. Phys.*, 2009, **130**, 034703.
67 C. J. Weststrate, R. Westerström, E. Lundgren, A. Mikkelsen and J. N. Andersen, *J. Phys. Chem. C*, 2009, **113**, 724.
68 C. J. Zhang, A. Michaelides, D. A. King and S. J. Jenkins, *J. Phys. Chem. C*, 2009, **113**, 6411.
69 A. Akita, S. Tanaka, K. Tanaka and M. Kohyama, *Mater. Sci. Forum*, 2010, **654**, 2362.
70 M. M. Branda, N. C. Hernández, J. F. Sanz and F. Illas, *J. Phys. Chem. C*, 2010, **114**, 1934.
71 T. s. Duchoň, F. Dvořák, M. Aulická, V. Stetsovych, M. Vorokhta, D. Mazur, K. i. Veltruská, T. s. Skála, J. Mysliveček, I. Matolínová and V. Matolín, *J. Phys. Chem. C*, 2013, **118**, 357.
72 Z. Lu, R. S. Feigelson, R. K. Route, S. A. DiCarolis, R. Hiskes and R. D. Jacowitz, *J. Cryst. Growth*, 1993, **128**, 788.
73 H. C. Aspinall, in *Rare Earth Oxide Thin Films: Growth, Characterization, and Applications*, ed. M. Fanciulli and G. Scarel, Springer Verlag, Berlin and Heidelberg, 2007, vol. 106, p. 53.
74 M. H. Zoellner, J. Dabrowski, P. Zaumseil, A. Giussani, M. A. Schubert, G. Lupina, H. Wilkens, J. Wollschläger, M. Reichling, M. Bäumer and T. Schroeder, *Phys. Rev. B: Condens. Matter Mater. Phys.*, 2012, **85**, 035302.
75 T. Staudt, Y. Lykhach, L. Hammer, M. A. Schneider, V. Matolín and J. Libuda, *Surf. Sci.*, 2009, **603**, 3382.
76 F. Dvořák, O. Stetsovych, M. Steger, E. Cherradi, I. Matolínová, N. Tsud, M. Škoda, T. Skála, J. Mysliveček and V. Matolín, *J. Phys. Chem. C*, 2011, **115**, 7496.
77 J. I. Flege, B. Kaemena, S. Gevers, F. Bertram, T. Wilkens, D. Bruns, J. Bätjer, T. Schmidt, J. Wollschläger and J. Falta, *Phys. Rev. B: Condens. Matter Mater. Phys.*, 2011, **84**, 235418.
78 P. Luches, F. Pagliuca and S. Valeri, *J. Phys. Chem. C*, 2011, **115**, 10718.
79 K. Mašek, J. Beran and V. Matolín, *Appl. Surf. Sci.*, 2012, **259**, 34.
80 S. D. Senanayake, J. T. Sadowski, J. Evans, S. Kundu, S. Agnoli, F. Yang, D. Stacchiola, J. I. Flege, J. Hrbek and J. A. Rodriguez, *J. Phys. Chem. Lett.*, 2012, **3**, 839.
81 O. Stetsovych, F. Dvořak, L. Szabová, S. Fabris, J. Mysliveček and V. Matolín, *Phys. Rev. Lett.*, 2012, **109**, 266102.

82 L. Szabová, O. Stetsovych, F. Dvořák, M. F. Camellone, S. Fabris, J. Mysliveček and V. Matolín, *J. Phys. Chem. C*, 2012, **116**, 6677.
83 J. I. Flege, B. Kaemena, S. D. Senanayake, J. Höcker, J. T. Sadowski and J. Falta, *Ultramicroscopy*, 2013, **130**, 87.
84 B. Kaemena, S. D. Senanayake, A. Meyer, J. T. Sadowski, J. Falta and J. I. Flege, *J. Phys. Chem. C*, 2013, **117**, 221.
85 P. Luches, F. Pagliuca, S. Valeri and F. Boscherini, *J. Phys. Chem. C*, 2013, **117**, 1030.
86 F. Pagliuca, P. Luches and S. Valeri, *Surf. Sci.*, 2013, **607**, 164.
87 J. I. Flege, B. Kaemena, J. Höcker, F. Bertram, J. Wollschläger, T. Schmidt and J. Falta, *Appl. Phys. Lett.*, 2014, **104**, 131604.
88 J. I. Flege, B. Kaemena, T. Schmidt and J. Falta, *J. Vac. Sci. Technol., B: Nanotechnol. Microelectron.: Mater., Process., Meas., Phenom.*, 2014, **32**, 03D124.
89 T. Schroeder, T. L. Lee, L. Libralesso, I. Joumard, J. Zegenhagen, P. Zaumseil, C. Wenger, G. Lupina, G. Lippert, J. Dabrowski and H. J. Mussig, *J. Appl. Phys.*, 2005, **97**, 074906.
90 A. Schaefer, T. Schroeder, G. Lupina, Y. Borchert, J. Dabrowski, C. Wenger and M. Bäumer, *Surf. Sci.*, 2007, **601**, 1473.
91 J. P. Liu, P. Zaumseil, E. Bugiel and H. J. Osten, *Appl. Phys. Lett.*, 2001, **79**, 671.
92 T. Weisemoeller, F. Bertram, S. Gevers, A. Greuling, C. Deiter, H. Tobergte, M. Neumann, J. Wollschläger, A. Giussani and T. Schroeder, *J. Appl. Phys.*, 2009, **105**, 124108.
93 B. Gehl, U. Leist, V. Aleksandrovic, P. Nickut, V. Zielasek, H. Weller, K. Al-Shamery and M. Bäumer, *Rev. Sci. Instrum.*, 2006, **77**, 083902.
94 A. Schaefer, S. Gevers, V. Zielasek, T. Schroeder, J. Falta, J. Wollschläger and M. Bäumer, *J. Chem. Phys.*, 2011, **134**, 054701.
95 S. Gevers, T. Weisemoeller, A. Schaefer, V. Zielasek, M. Bäumer and J. Wollschläger, *Phys. Rev. B: Condens. Matter Mater. Phys.*, 2011, **83**, 193408.
96 S. Gevers, T. Weisemoeller, B. Zimmermann, F. Bertram, C. Deiter and J. Wollschlager, *J. Phys.: Condens. Matter*, 2009, **21**, 8.
97 H. Wilkens, O. Schuckmann, R. Oelke, S. Gevers, M. Reichling, A. Schaefer, M. Bäumer, M. H. Zoellner, G. Niu, T. Schroeder and J. Wollschläger, *Phys. Chem. Chem. Phys.*, 2013, **15**, 18589.
98 E. J. Tarsa, J. S. Speck and M. Robinson, *Appl. Phys. Lett.*, 1993, **63**, 539.
99 H. J. Osten, J. P. Liu, E. Bugiel, H. J. Mussig and P. Zaumseil, *Mater. Sci. Eng., B*, 2001, **87**, 297.
100 N. M. Jeutter, W. Moritz, A. Sidorenko and A. Stierle, *Appl. Phys. Lett.*, 2007, **90**, 062906.
101 A. Schaefer, V. Zielasek, T. Schmidt, A. Sandell, M. Schowalter, O. Seifarth, L. E. Walle, C. Schulz, J. Wollschläger, T. Schroeder, A. Rosenauer, J. Falta and M. Bäumer, *Phys. Rev. B: Condens. Matter Mater. Phys.*, 2009, **80**, 045414.
102 T. Schroeder, P. Zaumseil, G. Weidner, W. Ch, J. Dabrowski, H. J. Müssig and P. Storck, *J. Appl. Phys.*, 2006, **99**, 014101.
103 T. Schroeder, P. Zaumseil, O. Seifarth, A. Giussani, H. J. Müssig, P. Storck, D. Geiger, H. Lichte and J. Dabrowski, *New J. Phys.*, 2008, **10**, 113004.
104 L. Eyring, in *Handbook of the Physics and Chemistry of Rare Earths*, ed. K. A. J. Gschneidner and L. Eyring, North-Holland, Amsterdam, 1979, ch. 337.
105 B. G. Hyde, E. E. Garver, U. E. Kuntz and L. Eyring, *J. Phys. Chem.*, 1965, **69**, 1667.
106 T. Weisemoeller, C. Deiter, F. Bertram, S. Gevers, A. Giussani, P. Zaumseil, T. Schroeder and J. Wollschläger, *Appl. Phys. Lett.*, 2008, **93**, 032905.
107 H. Wilkens, S. Gevers, S. Röhe, A. Schaefer, M. Bäumer, M. H. Zoellner, T. Schroeder and J. Wollschläger, *J. Phys. Chem. C*, 2014, **118**, 3056.
108 P. Zaumseil and T. Schroeder, *J. Phys. D: Appl. Phys.*, 2011, **44**, 055403.
109 C. L. Sieglaff and L. Eyring, *J. Am. Chem. Soc.*, 1957, **79**, 3024.
110 S. D. Park, J. M. Vohs and R. J. Gorte, *Nature*, 2000, **404**, 265.
111 B. C. H. Steele and A. Heinzel, *Nature*, 2001, **414**, 345.
112 M. A. Henderson, C. L. Perkins, M. H. Engelhard, S. Thevuthasan and C. H. F. Peden, *Surf. Sci.*, 2003, **526**, 1.
113 M. H. Zoellner, P. Zaumseil, H. Wilkens, S. Gevers, J. Wollschläger, M. Bäumer, Y.-H. Xie, G. Niu and T. Schroeder, *J. Cryst. Growth*, 2012, **355**, 159.
114 L. Vegard, *Z. Phys.*, 1921, **5**, 17.
115 J. D. McCullough, *J. Am. Chem. Soc.*, 1950, **72**, 1386.
116 G. Niu, P. Zaumseil, M. A. Schubert, M. H. Zoellner, J. Dabrowski and T. Schroeder, *Appl. Phys. Lett.*, 2013, **102**, 011906.
117 G. Niu, M. A. Schubert, F. d'Acapito, M. H. Zoellner, T. Schroeder and F. Boscherini, *Phys. Rev. B: Condens. Matter Mater. Phys.*, 2014, **116**, 123515.
118 J. M. D. Coey, M. Venkatesan and C. B. Fitzgerald, *Nat. Mater.*, 2005, **4**, 173.
119 N. Paunović, Z. Dohčević-Mitrović, R. Scurtu, S. Aškrabić, M. Prekajski, B. Matović and Z. V. Popović, *Nanoscale*, 2012, **4**, 5469.
120 G. Niu, E. Hildebrandt, M. A. Schubert, F. Boscherini, M. H. Zoellner, L. Alff, D. Walczyk, P. Zaumseil, I. Costina, H. Wilkens and T. Schroeder, *ACS Appl. Mater. Interfaces*, 2014, **6**, 17496.
121 J. M. Haschke and L. Eyring, *Inorg. Chem.*, 1971, **10**, 2267.
122 Z. Kang and L. Eyring, *J. Solid State Chem.*, 1988, **75**, 60.
123 H. Wilkens, J. Rodewald, S. Gevers, M. H. Zoellner, T. Schroeder and J. Wollschläger, *J. Phys. D: Appl. Phys.*, 2013, **46**, 285306.
124 S. Gevers, T. Weisemoeller, B. Zimmermann, C. Deiter and J. Wollschläger, *Phys. Status Solidi C*, 2010, **7**, 292.
125 J. V. Lauritsen and M. Reichling, *J. Phys.: Condens. Matter*, 2010, **22**, 263001.
126 S. Gritschneder and M. Reichling, *J. Phys. Chem. C*, 2008, **112**, 2045.
127 S. Torbrügge, J. Lübbe, L. Tröger, M. Cranney, T. Eguchi, Y. Hasegawa and M. Reichling, *Rev. Sci. Instrum.*, 2008, **79**, 083701.
128 A. Zangwill, *J. Cryst. Growth*, 1996, **163**, 8.

129 R. Cuerno, M. Castro, J. Muñoz-García, R. Gago and L. Vázquez, *Eur. Phys. J.: Spec. Top.*, 2007, **146**, 427.
130 M. Körner, F. Loske, M. Einax, A. Kühnle, M. Reichling and P. Maass, *Phys. Rev. Lett.*, 2011, **107**, 016101.
131 R. Olbrich, H. H. Pieper, R. Oelke, H. Wilkens, J. Wollschläger, M. H. Zoellner, T. Schroeder and M. Reichling, *Appl. Phys. Lett.*, 2014, **104**, 081910.
132 M. Kalff, P. Šmilauer, G. Comsa and T. Michely, *Surf. Sci.*, 1999, **426**, L447.
133 H. H. Pieper, C. Barth and M. Reichling, *Appl. Phys. Lett.*, 2012, **101**, 051601.
134 G. Ehrlich and F. G. Hudda, *J. Chem. Phys.*, 1966, **44**, 1036.
135 J. Krug, *Phys. A*, 2002, **313**, 47.
136 I. V. Markov, *Crystal growth for beginners: Fundamentals of nucleation, crystal growth and epitaxy*, World Scientific, 2008.
137 S. Gevers, T. Weisemoeller, D. Bruns, A. Giussani, T. Schroeder and J. Wollschläger, *J. Phys.: Condens. Matter*, 2011, **23**, 115904.
138 H. Wilkens, O. Schuckmann, R. Oelke, S. Gevers, A. Schaefer, M. Bäumer, M. H. Zoellner, T. Schroeder and J. Wollschläger, *Appl. Phys. Lett.*, 2013, **102**, 111602.
139 J. B. Goodenough, *Nature*, 2000, **404**, 821.
140 T. Hibino, A. Hashimoto, T. Inoue, J.-i. Tokuno, S.-i. Yoshida and M. Sano, *Science*, 2000, **288**, 2031.
141 M. Nakayama and M. Martin, *Phys. Chem. Chem. Phys.*, 2009, **11**, 3241.
142 S. Y. Chen, R. J. Chen, W. Lee, C. L. Dong and A. Gloter, *Phys. Chem. Chem. Phys.*, 2014, **16**, 3274.
143 M. H. Zoellner, G. Niu, J.-H. Jhang, A. Schaefer, P. Zaumseil, M. Bäumer and T. Schroeder, *J. Phys. Chem. C*, 2013, **117**, 24851.
144 M. P. Rosynek, *Catal. Rev.: Sci. Eng.*, 1977, **16**, 111.
145 Y. Tang, H. Zhang, L. Cui, C. Ouyang, S. Shi, W. Tang, H. Li, J.-S. Lee and L. Chen, *Phys. Rev. B: Condens. Matter Mater. Phys.*, 2010, **82**, 125104.
146 J. M. Tatibouët, *Appl. Catal., A*, 1997, **148**, 213.
147 M. Badlani and I. E. Wachs, *Catal. Lett.*, 2001, **75**, 137.
148 C. T. Au, W. Hirsch and W. Hirschwald, *Surf. Sci.*, 1989, **221**, 113.
149 C. Houtman and M. A. Barteau, *Langmuir*, 1990, **6**, 1558.
150 M. C. Wu, C. A. Estrada, J. S. Corneille and D. W. Goodman, *J. Chem. Phys.*, 1992, **96**, 3892.
151 P. A. Dilara and J. M. Vohs, *Surf. Sci.*, 1994, **321**, 8.
152 R. M. Ferrizz, G. S. Wong, T. Egami and J. M. Vohs, *Langmuir*, 2001, **17**, 2464.
153 A. Siokou and R. M. Nix, *J. Phys. Chem. B*, 1999, **103**, 6984.
154 D. R. Mullins, M. D. Robbins and J. Zhou, *Surf. Sci.*, 2006, **600**, 1547.
155 J. H. Beynon, A. E. Fontaine and G. R. Lester, *Int. J. Mass Spectrom. Ion Phys.*, 1968, **1**, 1.
156 S. D. Senanayake and D. R. Mullins, *J. Phys. Chem. C*, 2008, **112**, 9744.
157 Y. He, B. Yang and G. Cheng, *Catal. Today*, 2004, **98**, 595.
158 R. Juarez, P. Concepcion, A. Corma and H. Garcia, *Chem. Commun.*, 2010, **46**, 4181.
159 Y. Sun, Q. Liu, S. Gao, H. Cheng, F. Lei, Z. Sun, Y. Jiang, H. Su, S. Wei and Y. Xie, *Nat. Commun.*, 2013, **4**, 2899.
160 A. Younis, D. Chu, I. Mihail and S. Li, *ACS Appl. Mater. Interfaces*, 2013, **5**, 9429.
161 J. Zhang, H. Zhao, F. Wei, M. Yang, Z. Yang, Q. Chen and J. Chen, *Phys. Status Solidi RRL*, 2014, **8**, 95.
162 A. J. Jacobson, *Chem. Mater.*, 2009, **22**, 660.
163 N. Izu, W. Shin, N. Murayama and S. Kanzaki, *Sens. Actuators, B*, 2002, **87**, 95.
164 L. Liao, H. X. Mai, Q. Yuan, H. B. Lu, J. C. Li, C. Liu, C. H. Yan, Z. X. Shen and T. Yu, *J. Phys. Chem. C*, 2008, **112**, 9061.
165 V. Fernandes, P. Schio, A. J. A. de Oliveira, W. A. Ortiz, P. Fichtner, L. Amaral, I. L. Graff, J. Varalda, N. Mattoso, W. H. Schreiner and D. H. Mosca, *J. Phys.: Condens. Matter*, 2010, **22**, 216004.
166 M. C. Prestgard, G. Siegel, Q. Ma and A. Tiwari, *Appl. Phys. Lett.*, 2013, **103**, 102409.